

AD-A243 478



DTIC
ELECTE
DEC 7 1991
S C D

1

COARSENING OF δ' (Al_3Li) PRECIPITATES
IN ALUMINUM-LITHIUM ALLOYS

FINAL REPORT
(unclassified)

NAVAL AIR DEVELOPMENT CENTER
Contract No. N00019-82-C-0485

T. H. Sanders, Jr.
School of Materials Engineering
Purdue University
West Lafayette, IN 47907

April 1985

91-17196



EXEMPT FROM GDS
APPROVED FOR RELEASE
DISTRIBUTION UNLIMITED

91 17 196

REPORT DOCUMENTATION PAGE

Form Approved VM
OMB No. 0704-0188

Public reporting burden for this collection of information is estimated to average 1 hour per response, including the time for reviewing instructions, searching existing data sources, gathering and maintaining the data needed, and completing and reviewing the collection of information. Send comments regarding this burden estimate or any other aspect of this collection of information, including suggestions for reducing this burden, to Washington Headquarters Services, Directorate for Information Operations and Reports, 1215 Jefferson Davis Highway, Suite 1204, Arlington, VA 22202-4302, and to the Office of Management and Budget, Paperwork Reduction Project (0704-0188), Washington, DC 20503.

1. AGENCY USE ONLY (Leave blank)	2. REPORT DATE APRIL 1985	3. REPORT TYPE AND DATES COVERED FINAL	
4. TITLE AND SUBTITLE COARSENING OF δ'(Al_3Li) PRECIPITATES IN ALUMINUM-LITHIUM ALLOYS		5. FUNDING NUMBERS C N00019-82-C-C485	
6. AUTHOR(S) T. H. SANDERS, JR			
7. PERFORMING ORGANIZATION NAME(S) AND ADDRESS(ES) SCHOOL OF MATERIALS ENGINEERING PURDUE UNIVERSITY WEST LAFAYETTE, IN, 47907		8. PERFORMING ORGANIZATION REPORT NUMBER N00019-82-C-0485	
9. SPONSORING/MONITORING AGENCY NAME(S) AND ADDRESS(ES) NAVAL AIR DEVELOPMENT CENTER WARMINSTER, PA		10. SPONSORING/MONITORING AGENCY REPORT NUMBER	
11. SUPPLEMENTARY NOTES ALSO SEE LAST FINAL REPORT "PRECIPITATION MECHANICS IN ALUMINUM-LITHIUM ALLOYS", NAVAL AIR SYSTEMS COMMAND CONTRACT NO. N00019-81-C-0471, FINAL REPORT, SEPTEMBER 1983			
12a. DISTRIBUTION/AVAILABILITY STATEMENT APPROVED FOR PUBLIC RELEASE; DISTRIBUTION IS UNLIMITED		12b. DISTRIBUTION CODE	
13. ABSTRACT (Maximum 200 words) This final report is divided into four independently written sections: (1) Coarsening of δ'(Al_3Li) Precipitates in an Al-2.7Li-0.32Mn Alloy; (2) The influence of Zirconium on the Coarsening of δ'(Al_3Li) in an Al-2.7Li-0.14Zr Alloy; (3) The influence of δ'(Al_3Li) Volume Fraction on the Kinetics of δ' Coarsening and the Shape of the δ'(Al_3Li) Particle Size Distributions (PSD's); and (4) Preliminary Differential Scanning Calorimetry (DSC) Results in the Al-Cu-Mg-Li System.			
14. SUBJECT TERMS Aluminum-Lithium; Precipitates; Coarsening, Kinetics, Size, and Shape Distributions.		15. NUMBER OF PAGES 87	
		16. PRICE CODE	
17. SECURITY CLASSIFICATION OF REPORT UNCLASSIFIED	18. SECURITY CLASSIFICATION OF THIS PAGE UNCLASSIFIED	19. SECURITY CLASSIFICATION OF ABSTRACT UNCLASSIFIED	20. LIMITATION OF ABSTRACT UNLIMITED

FOREWORD

This final report is divided into four independently written sections.

1. Coarsening of δ' (Al_3Li) Precipitates in an Al-2.7Li-.32Mn Alloy.
2. The Influence of Zirconium on the Coarsening of δ' (Al_3Li) in an Al-2.7Li-0.14Zr Alloy.
3. The Influence of δ' (Al_3Li) Volume Fraction on the Kinetics of δ' Coarsening and the Shape of the δ' (Al_3Li) Particle Size Distributions (PSD's).
4. Preliminary Differential Scanning Calorimetry (DSC) Results in the Al-Cu-Mg-Li System.



Accession For	
NTIS GRA&I	<input checked="" type="checkbox"/>
DTIC TAB	<input type="checkbox"/>
Unannounced	<input type="checkbox"/>
Justification	
By _____	
Distribution/	
Availability Codes	
Dist	Avail and/or Special
A-1	

SUMMARY

The first section of this report describes the results of a quantitative transmission electron microscopy (TEM) investigation of the precipitation process of the metastable δ' (Al_3Li) phase in Al-2.7 wt% Li-0.3 wt% Mn. Isothermal aging times were varied from 12 hours to 12 weeks at three aging temperatures: 168°, 200°, and 225°C. Particle size distributions (PSD's) were determined for various aging times at the three aging conditions. The growth of δ' was found to obey Ostwald ripening kinetics. A symmetrical distribution was found to more closely approximate the experimental PSD's rather than the negatively skewed or log-normal distribution, predicted by many of the Ostwald ripening theories. These results were presented in the last final report "Precipitation Mechanics in Aluminum-Lithium Alloys," Naval Air Systems Command Contract No. N00019-81-C-0471, Final Report, September 1983; however, they have been further analyzed in this report and considered in light of the current theories of coarsening.

The second section describes the results of the influence of zirconium on the coarsening behavior of δ' . The results clearly show that the δ' nucleates on the pre-existing Al_3Zr particles. The nucleation on these particles was shown to affect the intercept of the \bar{R}^3 versus time relationship of the particles containing the Al_3Zr but not the Al_3Li particles not containing Al_3Zr . The presence of Zr affects the PSD's of all δ' particles not just the ones which contain Al_3Zr . Furthermore, the contrast of the Al_3Zr , Al_3Li precipitates indicates that the Al_3Zr precipitates are not completely ordered as has been previously suggested.

The third section describes the coarsening in a series of binary Al-Li alloys. The nominal compositions were: from Al-3Li to Al-4.5Li. Aging was carried out at 200° and 225°C on these systems and compared to the results presented in Section 1 of this report. From this systematic study it was observed that increasing the volume fraction

of δ' by increasing the amount of lithium in the alloy increased the rate of coarsening at a given aging time and temperature, and that as the volume fraction of δ' changes, the shape of the PSD changes. In dilute alloys the distribution function is asymmetrical and negatively skewed, and becomes more symmetrical with increasing δ' and in the high volume fraction alloy (Al-5Li), the PSD is asymmetrical, but positively skewed.

The fourth section summarizes the first experimental DSC results on the Al-Li-Cu-Mg alloys.

SECTION I. - LIST OF TABLES

- TABLE I-1. Composition of the Al-Li Alloy (given in weight percent)
- TABLE I-2. Aging Conditions Used for the Determination of Particle Size Distribution (PSD) Functions
- TABLE I-3. Number of Precipitates Examined at 168°C
- TABLE I-4. Number of Precipitates Examined at 200°C
- TABLE I-5. Number of Precipitates Examined at 225°C
- TABLE I-6. Experimental Values Determined From Figure 8 Based on Equation 1
- TABLE I-7. Values Determined From Figure 9 Based on Equation 3
- TABLE I-8. Results of the χ^2 Tests on the Application of the Normal Distribution to Approximate the PSD's
- TABLE I-9. The Effect of Aging Time at 168°C On the Mean Particle Diameter, \bar{D} , and the Standard Deviation, s , of the PSD
- TABLE I-10. The Effect of Aging Time at 200°C On the Mean Particle Diameter, \bar{D} , and the Standard Deviation, s , of the PSD
- TABLE I-11. The Effect of Aging Time at 225°C On the Mean Particle Diameter, \bar{D} , and the Standard Deviation, s , of the PSD

SECTION I. - LIST OF FIGURES

- FIGURE I-1. Theoretical particle size distributon (PSD) based on the LSW theory, from [I-4, I-5].
- FIGURE I-2. Theoretical PSD based on the MLSW theory with different volume fraction of precipitate, from [I-6].
- FIGURE I-3. Theoretical PSD based on the LSEM theory with two different volume fractions of precipitate, from [I-8].
- FIGURE I-4. Histogram of the δ' particles aged 2 weeks at 200°C.
- FIGURE I-5. PSD with generated normal curve.
- FIGURE I-6. Relation between \bar{R}^3 and time based on Equation (I-1).
- FIGURE I-7. Relation between \bar{R} with time^{1/3} based on Equation (I-3).
- FIGURE I-8. Histogram of δ' particles aged 1 week at 200°C.
- FIGURE I-9. Normalized histogram of the δ' particles aged 2 weeks at 200°C.
- FIGURE I-10. Combined PSD from the 168, 200, and 225°C aged microstructures.
- FIGURE I-11. Comparison of the combined PSD with the PSD from the Al-Li alloy aged 48 hours at 200°C.
- FIGURE I-12. Comparison of the combined PSD with the PSD from the Al-LI alloy aged for 8 weeks at 200°C.
- FIGURE I-13. Linear relationship between the standard deviation, s , and the mean particle diameter, \bar{D} .
- FIGURE I-14. Cumulative distribution of the aspect ratios of δ' .
- FIGURE I-15. Schematic illustrating the A and B positions on a (100) plane in an LI_2 structure at two different positions.
- FIGURE I-16. Illustration of two growing δ' precipitates.
- FIGURE I-17. Illustration of particle formed by the encounter of two particles, forming an antiphase domain boundary (APB).

SECTION I.

COARSENING OF δ' (Al₃Li) PRECIPITATES IN AN Al-2.7Li-.32Mn ALLOY

INTRODUCTION

Coarsening Theory

The ideas of precipitate coarsening were first formulated by Ostwald [I-1] in 1900. The coarsening process or Ostwald ripening as it is often called, describes the change of the average particle size with increasing time while the number of the dispersed phase particles decreases to maintain a constant volume fraction of precipitate. Observations show that during the coarsening process the larger particles grow at the expense of the smaller ones, and a particle size distribution (PSD) develops following some kind of pattern regardless of the initial PSD. The driving force for the coarsening process is the reduction in the free energy associated with the decrease in surface area of the particles during growth.

Because of the importance of precipitate stability in commercial alloys the coarsening process has been studied theoretically and experimentally by numerous investigators. Zener [I-2] and Greenwood's [I-3] pioneering work on this subject pointed out that coarsening is a diffusion-controlled process and they developed a relationship which showed the change of particle size is proportional to $(Dt)^{1/2}$ and $t^{1/3}$, respectively. In these relationships D refers to the diffusivity and t the time.

In 1961, Lifshitz, Slyozov [I-4] and Wagner [I-5] established a unified theoretical analysis (LSW theory) which incorporated the diffusion, continuity, and mass balance equations together, giving a result of $R \propto t^{1/3}$. These authors also showed a theoretical asymmetrical PSD, and described the effect of volume fraction, elastic strain, and anisotropy on the coarsening process. Unfortunately, there is a great disparity between either the theoretical PSD or the effect of volume fraction on the experimentally determined PSD's. Therefore, modifications [I-6 - I-8, I-12] have been made in order to

produce a better fit of theoretical PSD's to actual experimental PSD's. Ardell [I-6], for example, advanced a modified LSW theory (MSLW theory) in 1972. Introducing the influence of precipitate volume fraction into the diffusion equation by using a modified diffusion geometry, Ardell showed that the change of R is still proportional to $t^{1/3}$ however the growth rate of the particles increases as the volume fraction increases. Comparison of Ardell's theory with experimental data indicates that his model overestimates the influence of the volume fraction on coarsening.

Since 1972 new models and modifications have been presented [I-7,I-8]. For example, in 1980, the possibilities of particle encounters (particle coalescence) in systems containing large volume fractions of precipitates was presented by Davies, Nash and Stevens [I-8]. Their model is referred to as the Lifshitz-Slyozov encounter modified (LSEM) theory. Their predicted PSD's and average growth rates are in good agreement with experimental data. These PSD's tend to be symmetric about a mean value. The shapes of the theoretical PSD's for the different theories are presented in Figures I-1 - I-3. In these figures the abscissa is the ratio of the calculated precipitate size to the average precipitate size and the ordinate is the frequency of occurrence of a particular ratio. There are, however, two features which all the recent theories have in common. All theories reduce to the LSW theory in the limit of zero volume fraction of precipitate, and they predict a linear relationship of the mean particle size cubed versus the aging time.

Because of the importance and the number of recently published theoretical analyses on the coarsening process an experimental study of the coarsening process in a model system would be timely.

Precipitation in Al-Li Alloys

When Al-Li alloys with sufficient solute are quenched from the single phase field and subsequently aged below the critical temperature that defines the metastable miscibility gap, decomposition of the supersaturated solid solution occurs by homogeneous precipitation of the ordered $L1_2$ phase $Al_3Li(\delta')$ [I-9 - I-11]. The similarity in crystal structure and lattice parameter of the δ' and the fcc matrix results in a small misfit strain [I-12] and spherical precipitates. Subsequent coarsening of the δ' precipitates has been described by LSW coarsening kinetics [I-9 - I-11] with the average radius varying as $(\text{time})^{1/3}$.

Because the Al-Li system contains spherical precipitates with little strain, it makes an ideal system to study coarsening. This paper will present experimental PSD's from δ' precipitate measurements in Al-2.8Li-3Mn and compare the form of the PSD's to those presented in various models of Ostwald ripening. The linear relationship of the mean particle size cubed versus aging time for δ' will also be examined.

EXPERIMENTAL PROCEDURE

An aluminum-lithium alloy of composition described in Table I-1 was cast, hot and cold rolled to a thickness of 2.5 mm. The rolled sheet was then sectioned into 1 cm x 1 cm pieces. The sectioned samples were solution heat treated for 1/2 hour at 550°C in a noncorrosive salt bath and then quenched in cold water.

The samples were aged for different periods of time ranging from 12 hours to 12 weeks at three temperatures: 168°C, 200°C, and 225°C. The aging conditions are summarized in Table I-2. The samples were prepared for both optical and transmission electron microscopy (TEM).

Central dark field (CDF) images were found to give good contrast between images of the δ' precipitates and the matrix. Lattice images were formed on selected samples to determine the nature of the δ' precipitates.

Particle size measurements were made directly from the negatives using a semi-automatic EyeCom II image analyzing system. The EyeCom II is interfaced with a DEC PDP-11 minicomputer which was programmed to collect, store, and manipulate the raw data.

RESULTS

The structure, as determined by optical microscopy, was fully recrystallized with a grain size of approximately ASTM 5 (3910 grains/mm³). TEM revealed the presence of the ordered Al₃Li precipitates (δ') and also the larger, incoherent Al₆Mn dispersoids.

By taking a number of TEM micrographs at a particular aging condition and compiling all the measurements, a PSD was constructed. An example of a PSD is shown in Figure I-4. The number of particles counted per aging condition are summarized in Tables I-3 - I-5. In order to compare the experimental PSD's to a normal distribution, a numerical analysis of the data was employed. An example is shown in Figure I-5 where the open circles represent the data and the solid line the fitted normal curve.

To determine if antiphase boundaries (APB's) were present in individual precipitates, lattice images were formed using the $(100)_{\delta'}$, (000) and $(\bar{1}00)_{\delta'}$. Inspection of the lattice images did not reveal any antiphase boundaries.

DISCUSSION

Examination of the TEM foils at the different conditions revealed that the precipitates remained coherent and roughly spherical through the aging conditions investigated. These qualities make this system ideal for examining in detail the phenomenon of Ostwald ripening and for relating the data to theories in the literature.

While models for ripening may disagree on the form of the theoretical PSD, there is complete agreement on the functional dependence of the mean particle size \bar{R} versus aging time for diffusion controlled growth. The equation is of the form:

$$\bar{R}^3 - R_{CO}^3 = Kt \quad [I-1]$$

with R_{CO} the initial critical size for growth, and K a rate constant incorporating temperature, surface tension between particle and matrix, the equilibrium solute concentration, and the molar volume. K in Equation I-1 is defined by the relationship:

$$K = \frac{8 s D C_e V_m}{9RT} \quad [I-2]$$

where D is the diffusion coefficient of solute within the matrix, C_e the equilibrium solute concentration of the matrix at the aging temperature T , s the interfacial free energy of the precipitate, and V_m the molar volume of the precipitate.

Plotting the experimental values for the cube of the radii versus aging time, as required by Equation I-1, produces a plot as shown in Figure I-6. The values for the constants K and R_{CO} are found in Table I-6.

Examining the extrapolated values of R_{CO} , no systematic positive or negative values were observed. The values of R_{CO} are located around $R_{CO} = 0$, which has been identified by other workers in this system [I-9, I-10] to be a reasonable value for R_{CO} .

When R_{CO} is taken to be zero, or when $R_{CO} \ll R$, Equation I-1 reduces to

$$\bar{R} = K t^{1/3} \quad [I-3]$$

The average particle size versus $t^{1/3}$ for the different experimental conditions are plotted in Figure I-7. A "least-squares" line is included on the plot. The extrapolation to $t = 0$ of the "least-squares" lines are summarized in Table I-7. The intercept values are approximately zero suggesting that the assumption

$$\bar{R} \propto t^{1/3} \quad [I-4]$$

was reasonable. For the Al-Li system this result implies that the precoarsening regime is very short or does not exist at all.

TEM method for size measurements appears to be satisfactory over the range of particle sizes examined in this research, where the *matrix/particle interface* is well resolved and the precipitate overlap is small. However, further work at shorter aging times cannot be accomplished easily using TEM due to statistical sampling problems but will require small angle scattering techniques, for example.

Inspection of the various PSD's indicated that the distributions may be better described by a normal distribution rather than the log-normal distribution predicted by the LSW theory. Therefore, the model that the distribution function could be represented by a normal distribution was examined using the χ^2 test. The results of the χ^2 test are summarized in Table I-8. For a majority of the aging conditions investigated a normal distribution could be used to model the PSD's. A representative set of data in which the normal distribution satisfies the χ^2 criterion is illustrated in Figure I-5. Alternatively a set of data in which the χ^2 test indicated that the normal distribution was not an appropriate function to describe the distribution is shown in Figure I-8.

Although all the data did not strictly fit the criterion of accepting the normal distribution hypothesis close inspection of Figure I-8 and Table I-8 might suggest it could be used. For example in Table 8 several of the replicated samples were divided as to whether they accepted or rejected the hypothesis.

An alternative method of examining the PSD's is to plot the normalized frequency (that is, the frequency of a particular class interval is divided by the frequency from the class interval with the highest frequency, then multiply that result by 100), versus the normalized diameter (D/\bar{D}). This type of relationship is shown in Figure I-9. The normalized data set shown in Figure I-9 is the same data as shown in Figure I-4. This normalizing procedure was followed for each data set. Inspection of the resulting normalized histograms revealed that they were virtually identical in form. Therefore a composite distribution function was constructed to represent the sum of all the data. The composite distribution was constructed by summing the frequencies of a particular normalized class interval over all the data sets. This composite histogram is shown in Figure I-10.

In order to compare the composite distribution with the individual normalized distribution, the frequency was normalized according to the scheme outlined above. Figures I-11 and I-12 compare the normalized distribution for the combined data with the 48 hours at 200°C aging data, and the combined data with 8 weeks at 200°C aging data, respectively. These two aging times were used since they represented the minimum and maximum aging times investigated at 200°C. There is good agreement between the form of the composite distribution and the individual distribution.

To determine if a functional relationship existed between the average particle size, \bar{D} , and the standard deviation, s , of the distributions we examined this relationship as shown in Figure I-13. It is apparent from Figure I-13 that a simple linear relationship exists between s and \bar{D} . Using linear regression analysis and a model of the form:

$$s = m\bar{D} + b, \quad [I-5]$$

where m and b are the constants to be evaluated, the analytical expression:

$$s = 0.272\bar{D} - 2.22 \quad [I-6]$$

was determined. This relationship indicates that the PSD depends only on the extent of aging or the integrated effect of time and temperature. Thus, the PSD can be calculated from \bar{D} by this simple expression and assuming a normal PSD.

A further simplification of the above analysis can be made. Since the constant b is small, one can force the constant to be zero, and use the average of s/\bar{D} , (Tables I-9 - I-11) as the slope. From our data this simplified relationship is:

$$s = 0.268\bar{D}. \quad [I-7]$$

If this simple relationship can be shown to be general for other Al-Li alloys it would permit the determination of the entire distribution by knowing only the average particle size, \bar{D} . The average value of the diameter is easier to determine than the complete PSD.

Comparison of the experimental PSD's to various Ostwald ripening theories results in some interesting discrepancies. In all cases examined, the experimentally found PSD can be approximated by a normal distribution. This result is not predicted by all the theories.

The main foundation work of modern Ostwald ripening theory is the LSW theory [I-4, I-5]. The PSD predicted by this theory is illustrated in Figure I-1. This theoretically derived PSD is not symmetric, but rather log-normal. There is a cut-off at 1.5 times the mean particle size. Experimental observations in this research clearly show

that larger sizes do exist, and the distribution function is more symmetrical about the mean.

A modification of the theory, the MLSW (Modified Lifshitz-Slyozov-Wagner) theory, was proposed by Ardell [I-6]. The MLSW theory produced a theoretical PSD which incorporated the volume fraction of precipitates as a controlling parameter, producing theoretical PSD's of the form shown in Figure I-2 [I-6]. In this model, the theoretically determined PSD does approach symmetric behavior at volume fractions approaching unity. The MLSW model predicts a slightly asymmetric PSD, with a slight deviation of the maximum frequency value away from the mean particle size \bar{R} . Although this is a closer approximation to the experimental results presented in this investigation, the limitation of MLSW theory is that it overestimates the influence of volume fraction on the growth rate of particles [I-8].

Similarly, the model proposed by Brailsford and Wynblatt [I-7], which also depends upon volume fraction as a controlling parameter, predicts an asymmetric PSD and is thus inconsistent with the experimentally found PSD's. The asymmetry of the theoretical PSD represents a considerable problem which must be reconciled.

Of all the models surveyed, the LSEM (Lifshitz-Slyozov Encounter Modified) theory predicts symmetric PSD's and the existence of particles whose upper limit is twice the mean particle size [I-8]. The LSEM model takes into account the encounters between close precipitates to combine and form particles of volume fraction equal to the sum of the individual particle volume fractions. Lifshitz and Slyozov acknowledge encounters in their work but do not predict a symmetrical distribution, while MLSW and Brailsford-Wynblatt models do not consider these events to be significant. The LSEM theory describes the change in the theoretical PSD with the inclusion of encounters, broadening the PSD. This broadening of the curves can be seen in Figure I-3, as compared to the theoretical PSD's of the previously discussed theories. It is especially

important to note that values near two times the mean particle size are probable in the LSEM theory.

Since the idea of encounters is central to the LSEM theory, it must be considered in more detail. Encounters between precipitates may be identified in two different ways. Davies et al. identified encounters by the shape of the particles. For example, in micrographs taken of extraction replicas of a Ni-Co-Al alloy containing Ni_3Al type precipitates they showed many examples of particle contact illustrated by "L" shaped particles and necks between the particles. Consequently, one method is to examine the overall shape of individual particles. δ' precipitates are approximately spherical, producing an aspect ratio near 1.00, where the aspect ratio is defined as the ratio of the minor axis to the major axis. If an encounter occurs between two precipitates, this aspect ratio will deviate significantly from unity, producing a value of .50 when two identical dimension precipitates meet. The occurrence of particles with aspect ratios between .50 to .80 may indicate the possibility of an encounter. A cumulative distribution of aspect ratios is shown in Figure I-14. Less than 4% of measured particles had an aspect ratio less than .80. If an aspect ratio $< .80$ is used as a criterion of encounter events, the number of encounters is quite small and perhaps not significant.

The idea of encounters may also be examined in a different light. Consider two precipitates, as shown in Figure I-15, having an L1_2 structure like δ' , with the aluminum in the face center positions and the lithium in the corner positions. During aging, the precipitates will grow forming spherical precipitates, as shown in Figure I-16. If aging continues, the precipitates will continue to grow and the separate precipitates will meet and form a new, larger precipitate. Unless there is a lattice registry between the two precipitates, an antiphase domain boundary (APB) will form, shown in Figure I-17. In the FCC structure there is a 50-50 probability that an APB will form. The existence of some encounters might, therefore, be identified by the presence of an APB within a precipitate. If the LSEM model indeed fits the ripening of δ' precipitates, some APB's

should be found in some δ' precipitates. No APB's were found in any of the images examined, suggesting that if encounters occur between precipitates they might be limited to those precipitates which are in crystallographic registry.

The physical description of the coalescence model proposed by Davies et al. [I-8] has been recently questioned by Doherty on the grounds that it would be difficult to feed solute between the narrowing gap of the two coalescing precipitates [I-13]. As an alternative mechanism Doherty proposed that two precipitates are actually attracted toward one another and they move together. The driving force for this attraction is the removal of the elastically strained matrix lying between the two coherent precipitates and that increasing the precipitate/matrix misfit would increase the driving force for the reaction. To substantiate his model Doherty refers to the published results of a coarsening study reported by Rastogi and Ardell [I-14]. They found a relationship between the absolute value of the lattice misfit and the corresponding deviation of the experimental from the theoretical cut-off radii, $\rho = 1.5$ (see Figure I-1 for the cut-off of the LSW model). Increasing the absolute misfit broadened the PSD by increasing the observed cut-off.

In the case of Al-Li alloys the misfit is very low (the absolute value of the strain is less than 0.1%) [I-10] and yet the particle size distribution is broad with an observed cut-off of 1.75.

From our metallographic examinations it is therefore not evident that encounters as envisaged by the simple idea of spontaneous coalescence of two particles into one larger particle either by the model proposed by Davies et al. or that proposed by Doherty occurs in this particular Al-Li alloy. Although the coalescence may be a method to mathematically model the coarsening process and produce more realistic PSD's it does not appear to be the physical description by which we can account for the broad, symmetrical PSD's.

SUMMARY AND CONCLUSIONS

It was observed for an Al-2.8Li alloy the growth of δ' precipitates was found to obey an Ostwald ripening growth mechanism. The form of the experimental PSD's of δ' was determined to be a distribution function which may be approximated by a normal distribution.

An analytical expression of the form:

$$s = 0.268\bar{D}$$

was found to relate the standard deviation, s , of the PSD to the average particle size, \bar{D} .

In comparing the experimental results to various theories of Ostwald ripening, it was observed that none of the surveyed theories represented an accurate description of what occurred in this Al-Li system. The LSW, MLSW and Brailsford-Wynblatt models were unable to predict a symmetrical PSD. While the LSEM model does predict a symmetrical PSD, the lattice images and an analysis of the precipitate shape of the δ' particles does not support spontaneous coalescence of two particles as part of the coarsening process in this alloy.

REFERENCES

- I-1. W. Ostwald, *Z. Phys. Chem.*, *34*, 495 (1900).
- I-2. C. Zener, *J. Appl. Phys.*, *20*, 950 (1949).
- I-3. G. W. Greenwood, *Acta Met.*, *4*, 243 (1956).
- I-4. I. M. Lifshitz and V. V. Slyozov, *J. Phys. Chem. Solids*, *19*, 35 (1961).
- I-5. C. Wagner, *Z. Electrochem.*, *65*, 581 (1961).

- I-6. A. J. Ardell, *Acta Met.*, 20, 61 (1972).
- I-7. A. D. Brailsford and P. Wynblatt, *Acta Met.*, 27, 489 (1979).
- I-8. C. K. L. Davies, P. Nash and R. N. Stevens, *Acta Met.*, 28, 179 (1980).
- I-9. B. Noble and G. E. Thompson, *Metals Science Journal*, 5, 114 (1971).
- I-10. D. B. Williams and J. W. Eddington, *Metal Science*, 9, 529 (1975).
- I-11. T. H. Sanders, Jr., E. A. Ludwiczak, and R. R. Sawtell, *Materials Science Engineering*, 43, 247 (1980).
- I-12. P. Niskanen, T. H. Sanders, Jr., M. Marek and J. G. Rinker. *Aluminum-Lithium Alloys*, T. H. Sanders, Jr. and E. A. Starke, Jr., eds., AIME, Warrendale, PA (1981), 347.
- I-13. R. D. Doherty, *Metal Science*, 16, 1 (1982).
- I-14. P. K. Rastogi and A. J. Ardell, *Acta Met.*, 19, 321 (1971).

TABLE I-1.

COMPOSITION OF THE Al-Li ALLOY
(given in weight percent)

Li	Mn	Fe	Si	Al
2.78	0.32	0.06	0.04	Balance

TABLE I-2.

AGING CONDITIONS USED FOR THE DETERMINATION OF
PARTICLE SIZE DISTRIBUTION (PSD) FUNCTIONS

AGING TIME		TEMPERATURE		
		168°C	200°C	225°C
12 hours	4.32 x 10 ⁴ seconds	--	--	*
24 hours	8.64 x 10 ⁴ seconds	--	--	*
36 hours	1.30 x 10 ⁵ seconds	--	--	*
48 hours	1.73 x 10 ⁵ seconds	--	*	*
72 hours	2.59 x 10 ⁵ seconds	--	--	*
96 hours	3.46 x 10 ⁵ seconds	--	*	*
144 hours	5.18 x 10 ⁵ seconds	--	--	*
1 week	6.05 x 10 ⁵ seconds	*	*	--
8 days	6.91 x 10 ⁵ seconds	*	--	--
10 days	8.64 x 10 ⁵ seconds	*	--	--
274 hours	9.86 x 10 ⁵ seconds	--	*	--
2 weeks	1.21 x 10 ⁶ seconds	*	*	--
4 weeks	2.42 x 10 ⁶ seconds	*	*	--
6 weeks	3.63 x 10 ⁶ seconds	--	*	--
7 weeks	4.24 x 10 ⁶ seconds	*	--	--
8 weeks	4.84 x 10 ⁶ seconds	*	*	--
9 weeks	5.44 x 10 ⁶ seconds	*	--	--
10 weeks	6.05 x 10 ⁶ seconds	*	--	--
11 weeks	6.65 x 10 ⁶ seconds	*	--	--
12 weeks	7.26 x 10 ⁶ seconds	*	--	--

* Denotes PSD measurements conditions.

-- Denotes PSD measurement not made for these conditions.

TABLE I-3
NUMBER OF PRECIPITATES EXAMINED
AT 168°C

Aging Conditions (Time Aged)	Number of TEM Films Examined	Total Number of Precipitates Analyzed
1 week	3	390
1 week	6	1160
8 days	3	392
10 days	3	438
2 weeks	4	504
4 weeks	3	530
7 weeks	5	448
8 weeks	3	424
9 weeks	4	421
10 weeks	4	408
11 weeks	4	408
12 weeks	3	346

TABLE I-4
NUMBER OF PRECIPITATES EXAMINED
AT 200°C

Aging Conditions (Time Aged)	Number of TEM Films Examined	Total Number of Precipitates Analyzed
48 hours	5	665
96 hours	5	642
1 week	4	408
1 week*	5	391
274 hours	5	600
2 weeks	8	1317
4 weeks	8	709
6 weeks	10	793
8 weeks	8	563

* Represents duplicate sample.

TABLE I-5
**NUMBER OF PRECIPITATES EXAMINED
 AT 225°C**

Aging Conditions (Time Aged)	Number of TEM Films Examined	Total Number of Precipitates Analyzed
12 hours	6	726
24 hours	7	614
36 hours	9	1220
36 hours*	5	619
48 hours	6	777
48 hours*	8	724
72 hours	9	698
96 hours	7	697
96 hours*	5	668
144 hours	8	879
144 hours*	6	656

* Represents duplicate sample.

TABLE I-6
**EXPERIMENTAL VALUES DETERMINED FROM FIGURE 8
 BASED ON EQUATION 1**

T (°C)	$K \times 10^{-24} \text{cm}^3/\text{sec}$	$R_{Co}(\text{Å})$
168	2.524	-102
200	21.67	-130
225	85.13	108

TABLE I-7
**VALUES DETERMINED FROM FIGURE 9
 BASED ON EQUATION 3**

T (°C)	$K \times 10^{-8} \text{cm}/\text{sec}^{1/3}$	Intercept (Å)
168	1.21	18
200	2.80	-10
225	4.35	13

TABLE I-8.

RESULTS OF THE χ^2 TESTS ON THE APPLICATION OF THE NORMAL DISTRIBUTION TO APPROXIMATE THE PSD'S.

Aging Temp.	Aging Time	Standard Deviation	χ^2	H ₀
168	1 week	0.239	15.97	Y*
	1 week	0.248	70.41	*
	8 days	0.256	22.99	Y*
	10 days	0.257	29.90	Y(?)*
	2 weeks	0.246	48.67	*
	4 weeks	0.276	39.8	*
	7 weeks	0.267	25.2	Y*
	8 weeks	0.296	19.67	Y*
	9 weeks	0.306	18.37	Y*
	10 weeks	0.262	23.26	Y*
	11 weeks	0.284	39.08	*
	12 weeks	0.282	8.55	Y*
200	48 hours	0.262	11.42	Y**
	96 hours	0.263	22.27	**
	1 week	0.263	19.60	**
	1 week	0.260	30.95	**
	274 hours	0.266	9.32	Y**
	2 weeks	0.277	11.81	Y**
	4 weeks	0.280	13.75	Y**
	6 weeks	0.269	3.51	Y*
	8 weeks	0.252	23.12	Y*
225	12 hours	0.268	16.65	Y(?)**
	24 hours	0.267	2.21	Y**
	36 hours	0.262	45.68	**
	36 hours	0.242	18.08	Y(?)**
	48 hours	0.267	5.40	Y**
	48 hours	0.258	20.35	**
	72 hours	0.270	7.56	Y**
	96 hours	0.278	25.50	**
	96 hours	0.257	7.98	Y**
	144 hours	0.282	39.43	

Y(?) perhaps close to a normal distribution.

H₀ hypothesis true for normal distribution if $\lambda^2 < 27.59$ for 20 classes and $\lambda^2 < 14.07$ for 10 classes at 0.95 level of confidence.

* 20 classes

** 10 classes

TABLE I-9.
THE EFFECT OF AGING TIME AT 168°C ON THE MEAN PARTICLE
DIAMETER, \bar{D} , AND THE STANDARD DEVIATION, s , OF THE PSD.

Aging Time	\bar{D} (A)	s (A)	$\frac{s}{\bar{D}}$
1 week	275.	70.3	0.256
8 days	278.	71.5	0.257
10 days	238.	56.9	0.239
2 weeks	293.	72.7	0.248
2 weeks*	291.	71.6	0.246
4 weeks	337.	93.	0.275
7 weeks	441.	118	0.268
8 weeks	456.	135.	0.296
9 weeks	461.	141.	0.305
10 weeks	511.	134.	0.262
11 weeks	475.	135.	0.284
12 weeks	516.	145.	0.281

*Represents duplicate specimen.

TABLE I-10.
THE EFFECT OF AGING TIME AT 200°C ON THE MEAN PARTICLE
DIAMETER, \bar{D} , AND THE STANDARD DEVIATION, s , OF THE PSD.

Aging Time	\bar{D} (A)	s (A)	$\frac{s}{\bar{D}}$
48 hours	318.	83.4	0.262
96 hours	386.	101.	0.262
1 week	483.	127.	0.263
1 week*	441.	115.	0.261
274 hours	482.	128.	0.266
2 weeks	525.	145.	0.276
4 weeks	750.	210.	0.280
6 weeks	893.	240.	0.320
8 weeks	910.	229.	0.252

*Represents duplicate specimen.

TABLE I-11.

THE EFFECT OF AGING TIME AT 225°C ON THE MEAN PARTICLE DIAMETER, \bar{D} , AND THE STANDARD DEVIATION, s , OF THE PSD.

Aging Time	\bar{D} (A)	s (A)	$\frac{s}{\bar{D}}$
12 hours	343.	91.9	0.268
24 hours	400.	107.	0.268
36 hours	473.	124.	0.262
36 hours*	472.	114.	0.242
48 hours	498.	133.	0.267
48 hours*	519.	134.	0.258
72 hours	567.	153.	0.270
96 hours	633.	176.	0.278
96 hours*	643.	166.	0.258
144 hours	711.	200.	0.281
144 hours*	732.	197.	0.269

*Represents duplicate specimen.

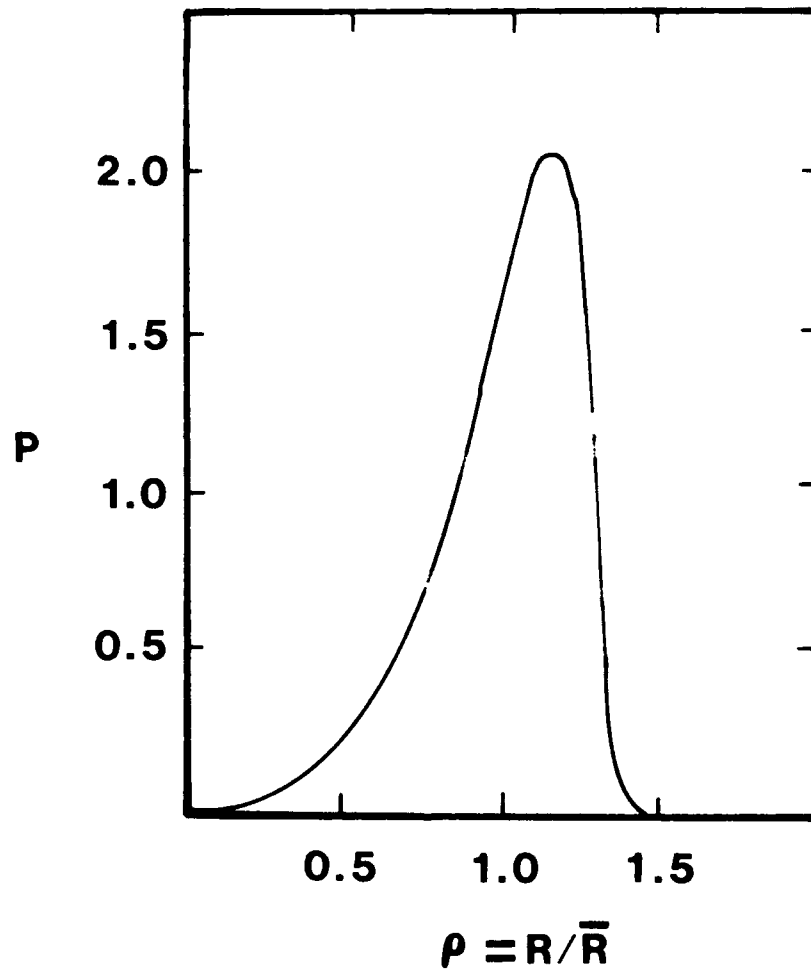


FIGURE I-1. Theoretical particle size distribution (PSD) based on the LSW theory, from [I-4, I-5].

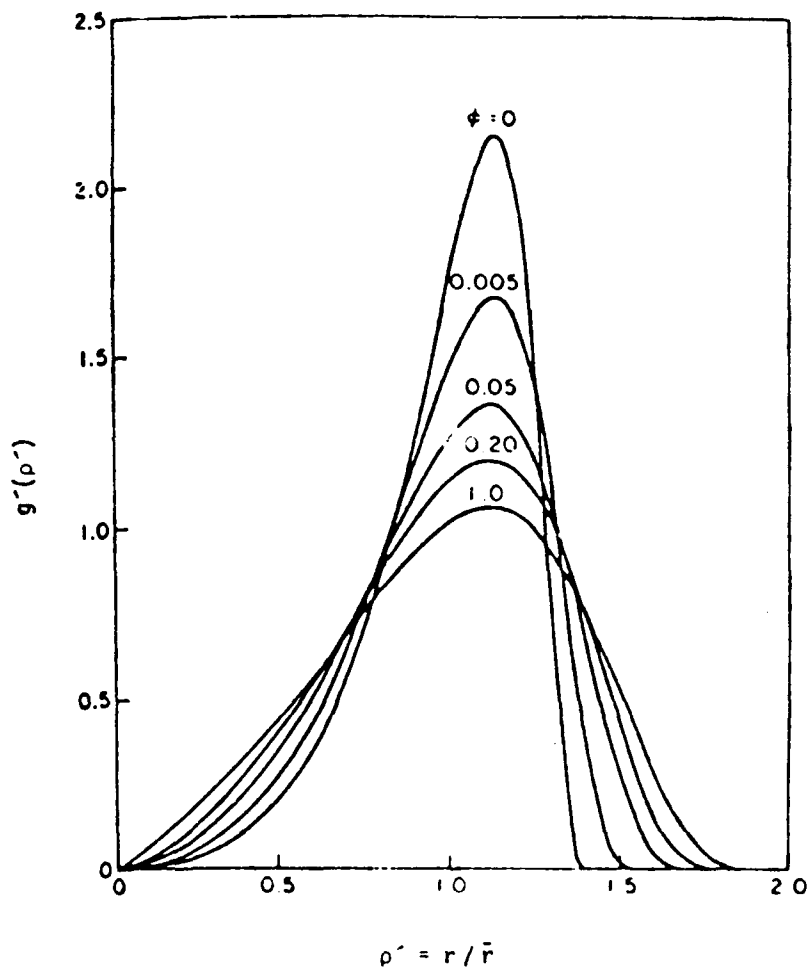


FIGURE I-2. Theoretical PSD based on the MLSW theory with different volume fraction of precipitate, from [I-6].

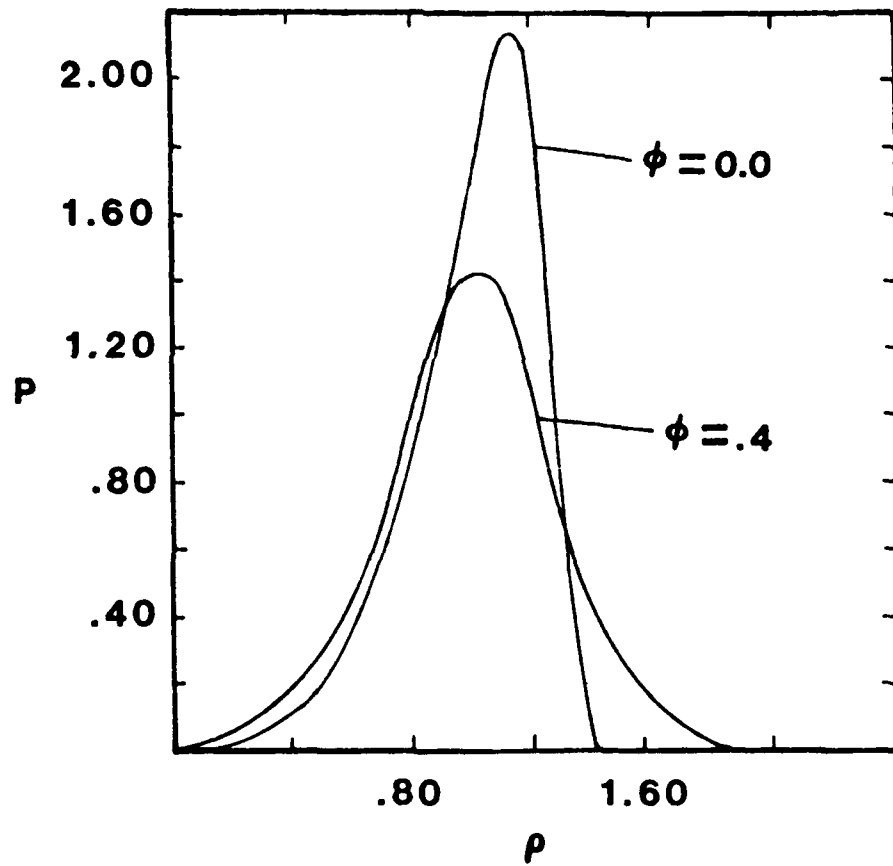


FIGURE I-3. Theoretical PSD based on the LSEM theory with two different volume fractions of precipitate, from [I-8].

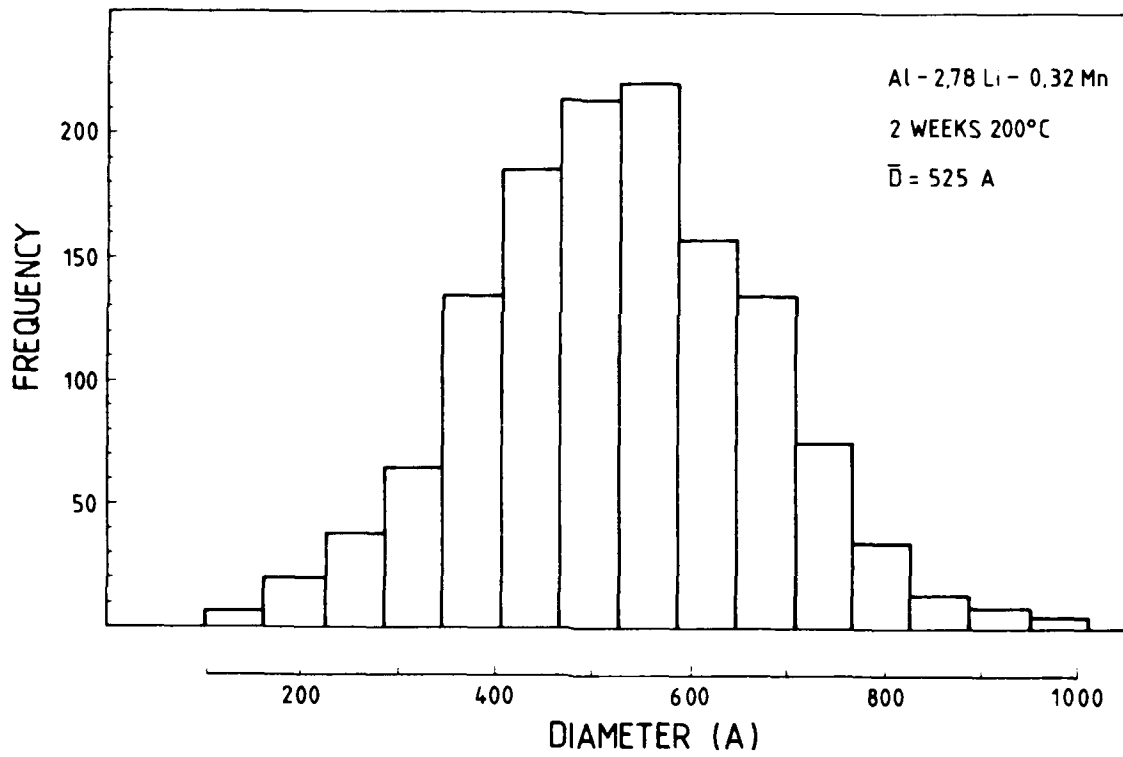


FIGURE I-4. Histogram of the δ' particles aged 2 weeks at 200°C.

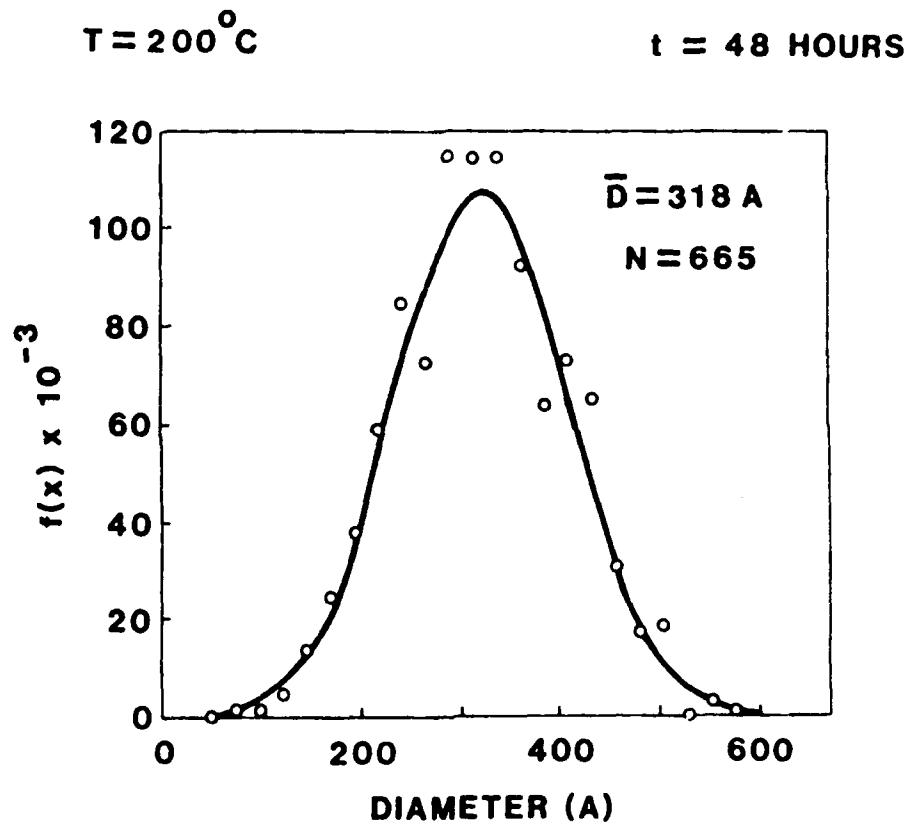


FIGURE I-5. PSD with generated normal curve.

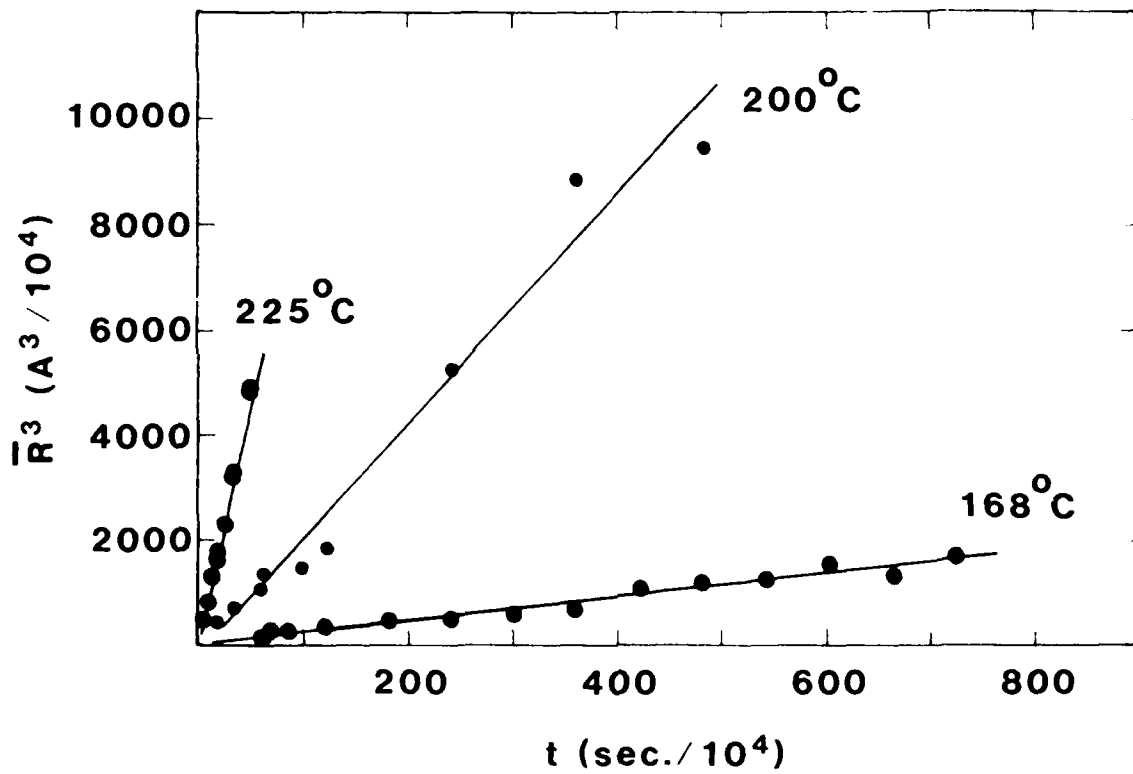


FIGURE I-6. Relation between \bar{R}^3 and time based on Equation (I-1).

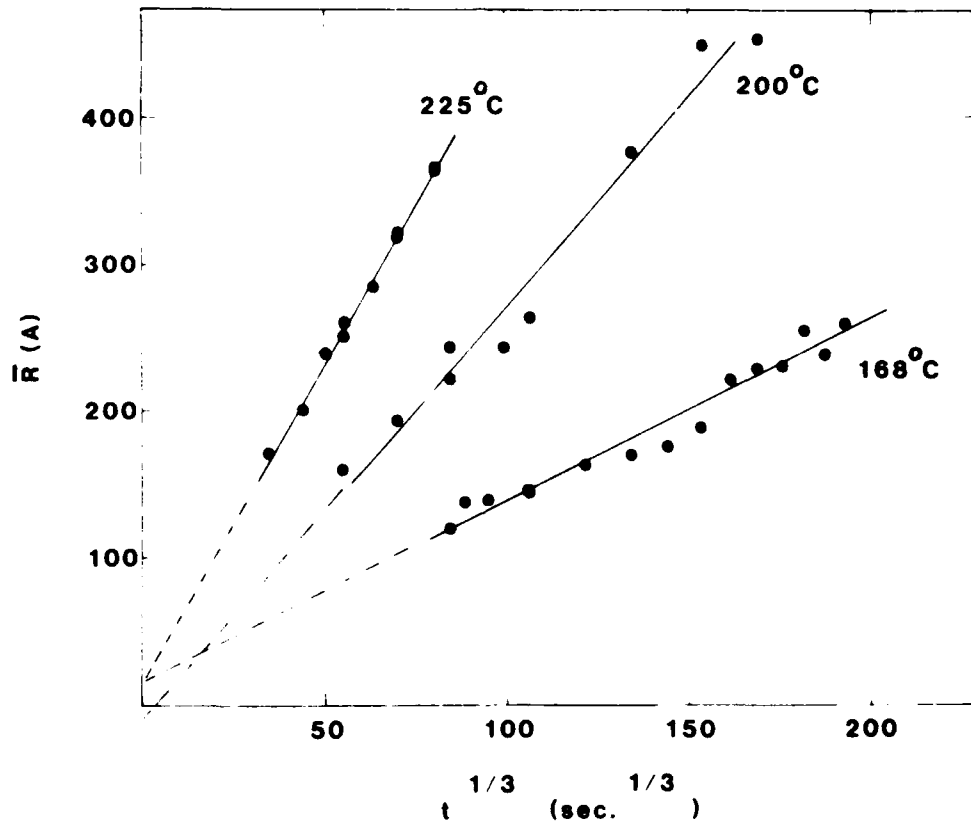


FIGURE I-7. Relation between \bar{R} with time $^{1/3}$ based on Equation (I-3).

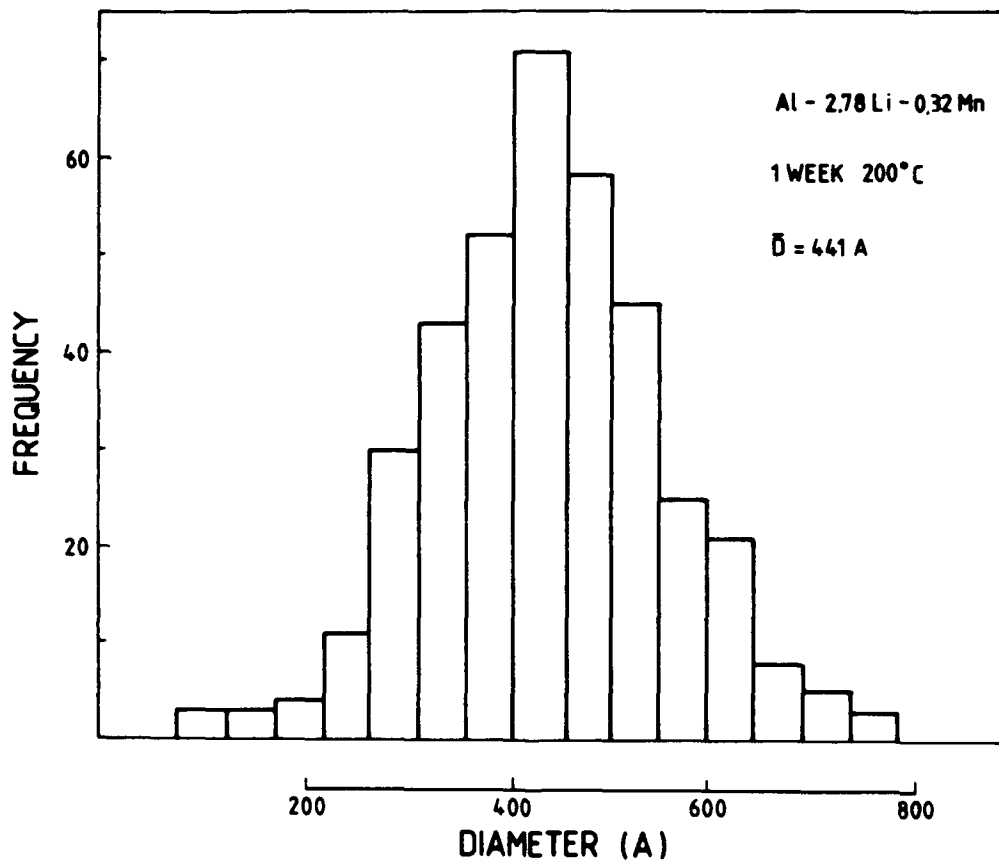


FIGURE I-8. Histogram of δ' particles aged 1 week at 200°C.

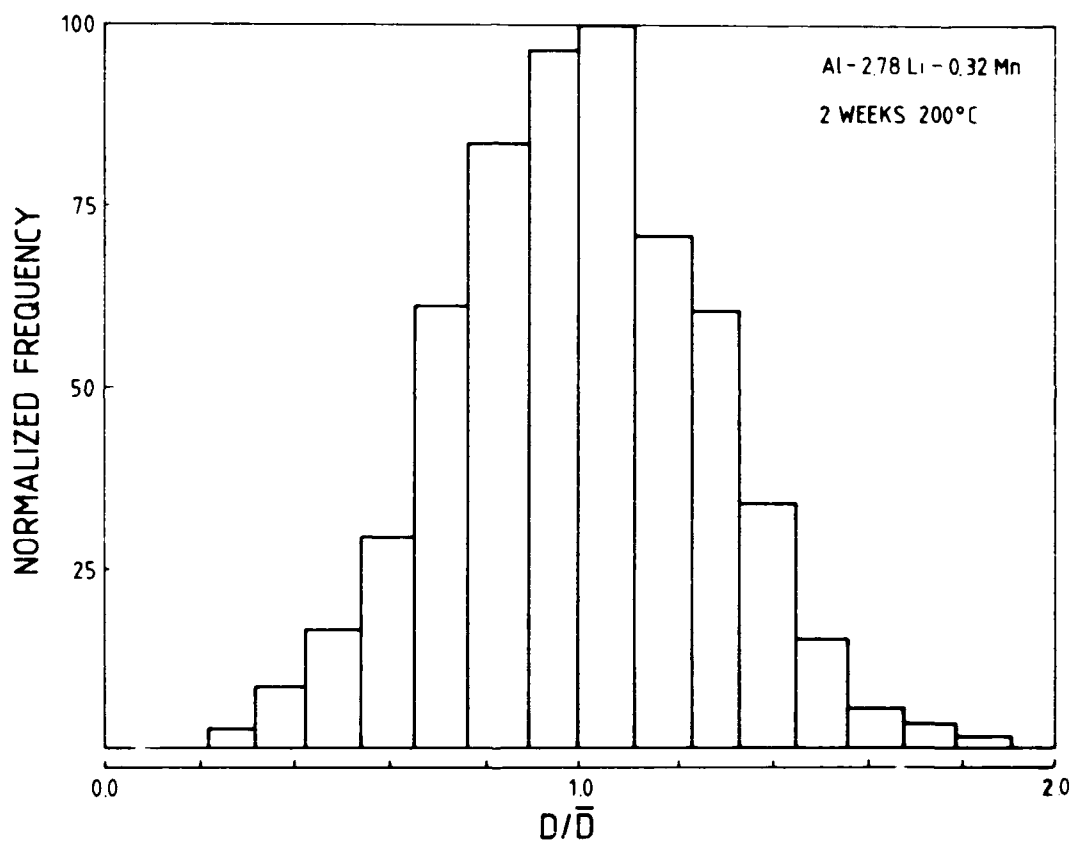


FIGURE I-9. Normalized histogram of the δ' particles aged 2 weeks at 200°C.

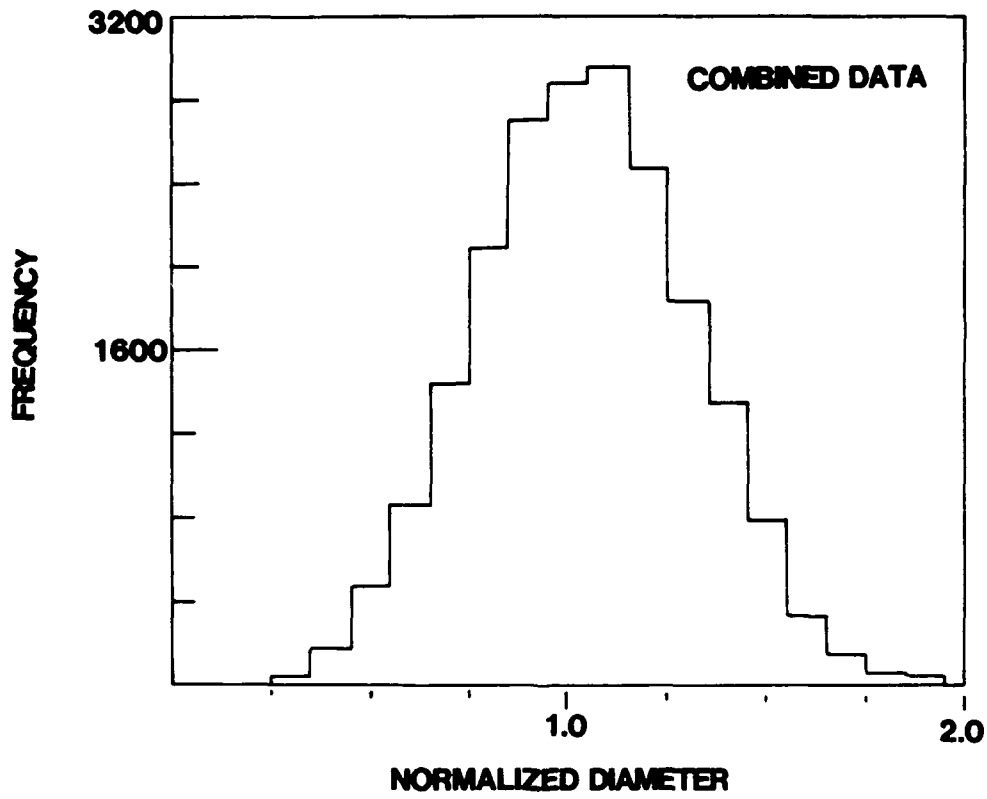


FIGURE I-10. Combined PSD from the 168, 200 and 225°C aged microstructures.

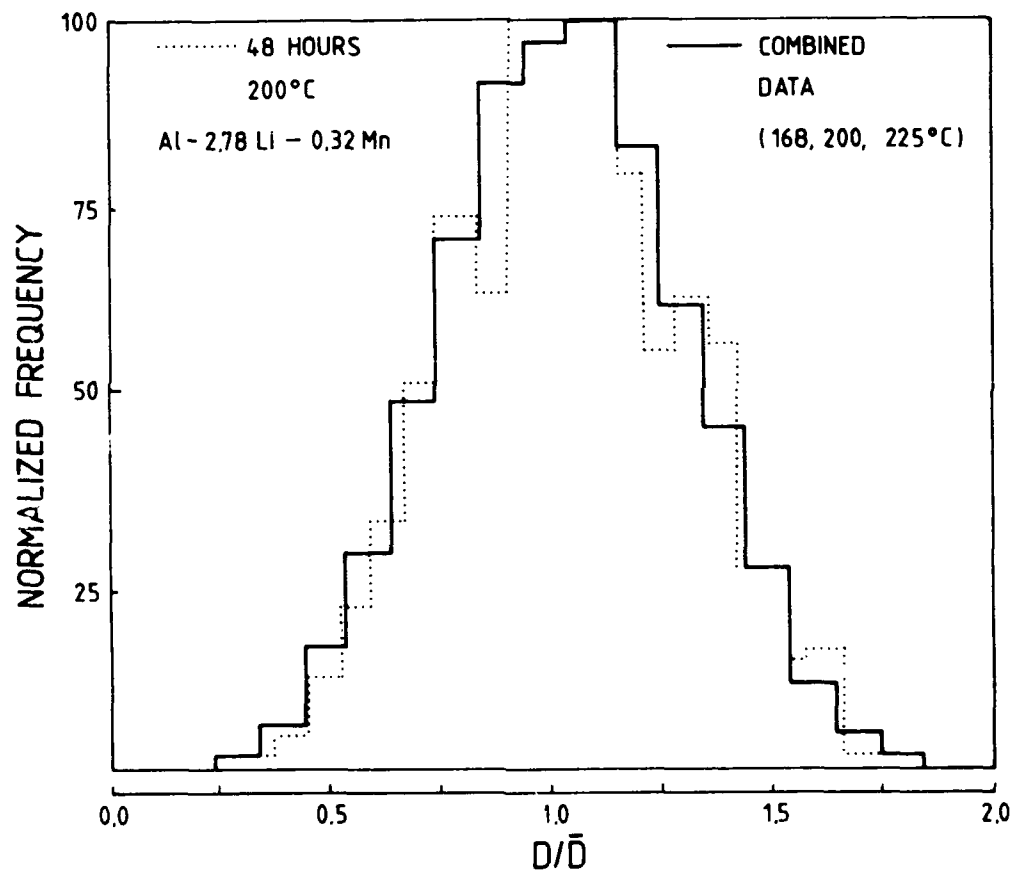


FIGURE I-11. Comparison of the combined PSD with the PSD from the Al-Li alloy aged 48 hours at 200°C.

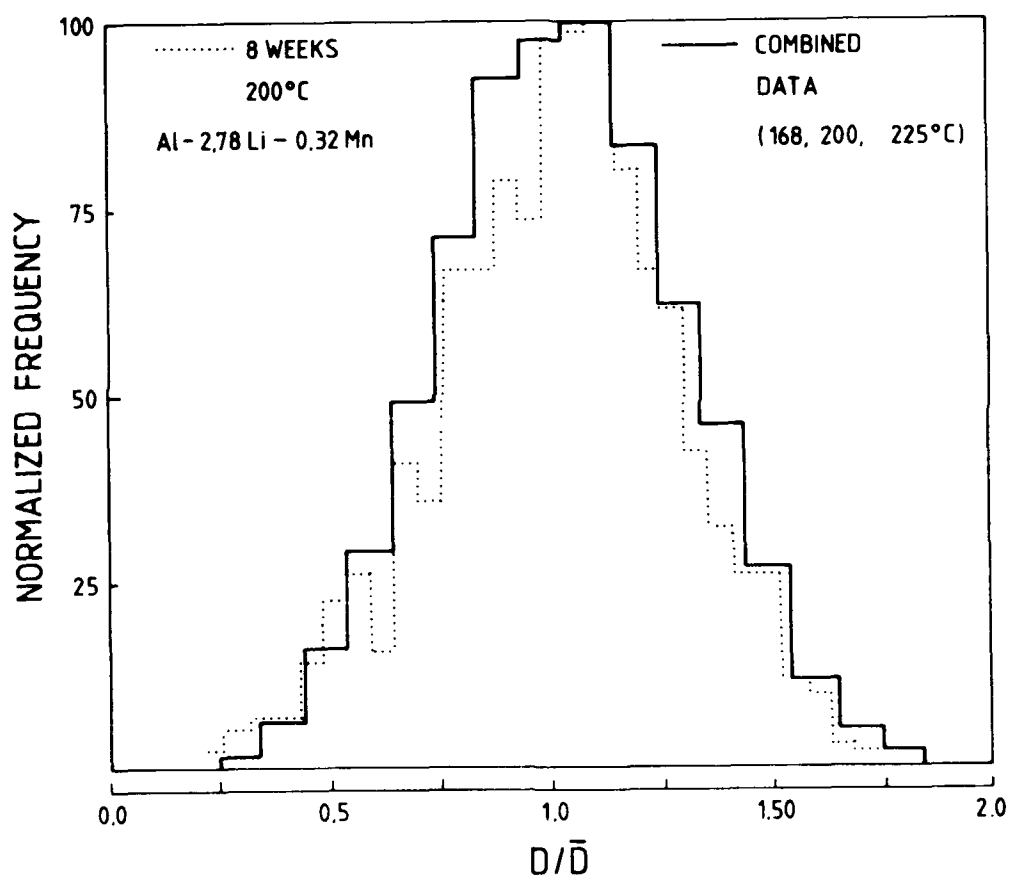


FIGURE I-12. Comparison of the combined PSD with the PSD from the Al-Li alloy aged for 8 weeks at 200°C.

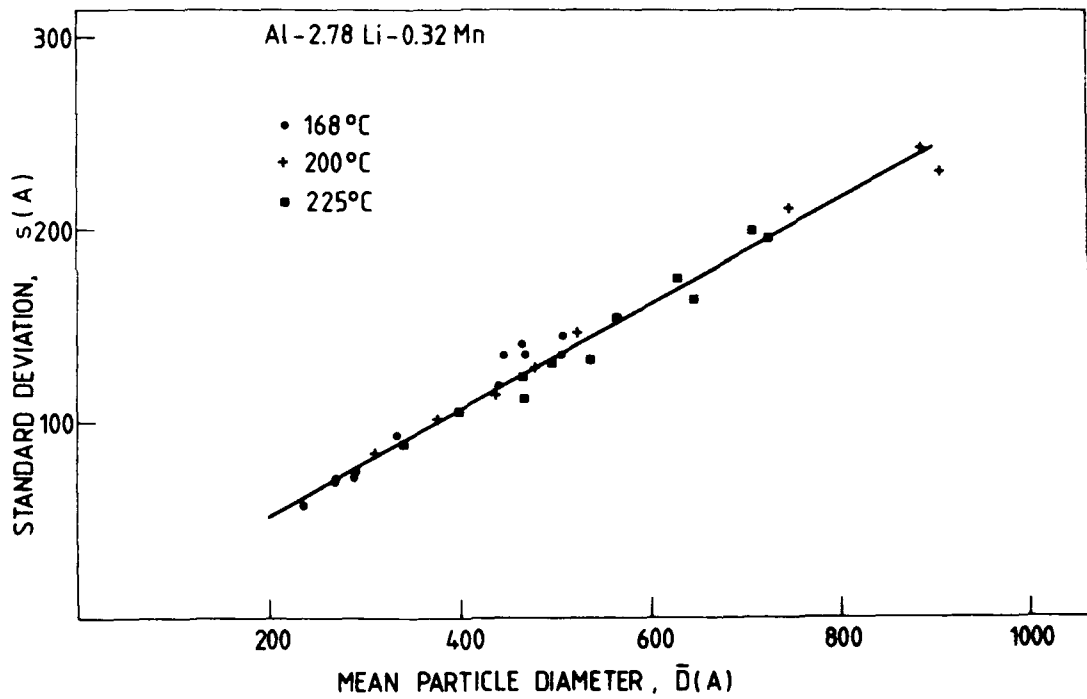


FIGURE I-13. Linear relationship between the standard deviation, s, and the mean particle diameter, \bar{D} .

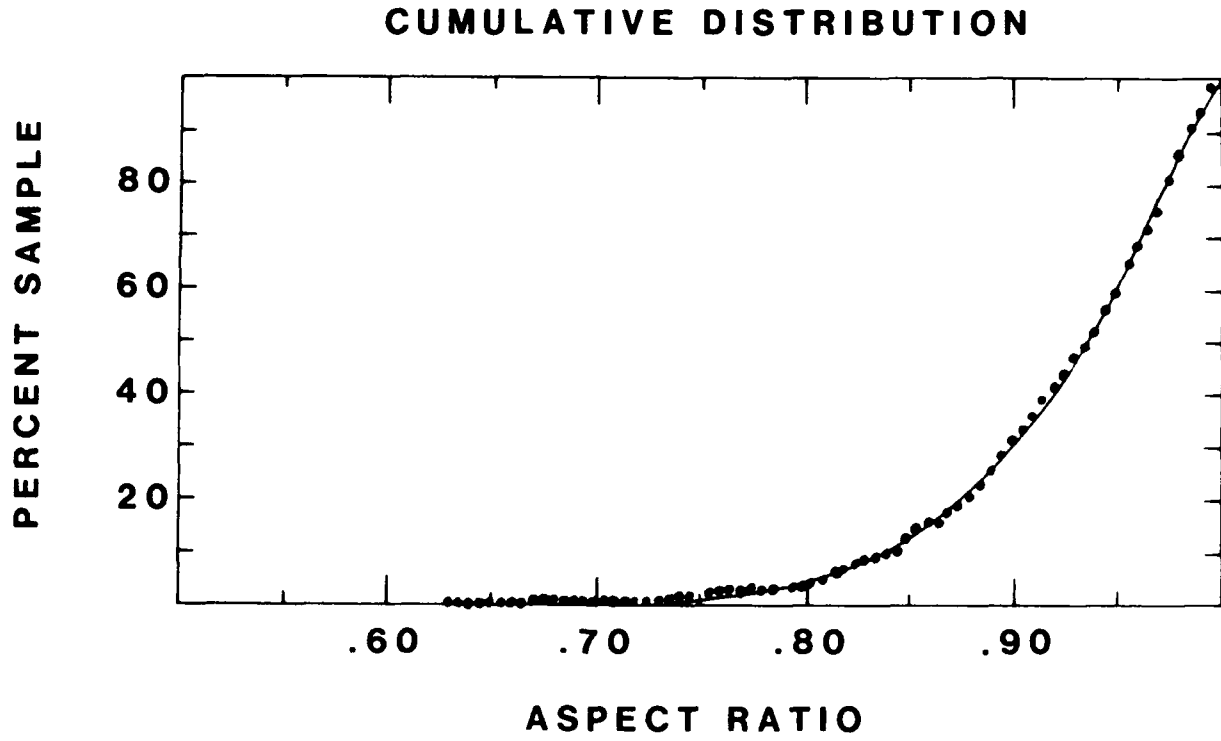


FIGURE I-14. Cumulative distribution of the aspect ratios of δ' .

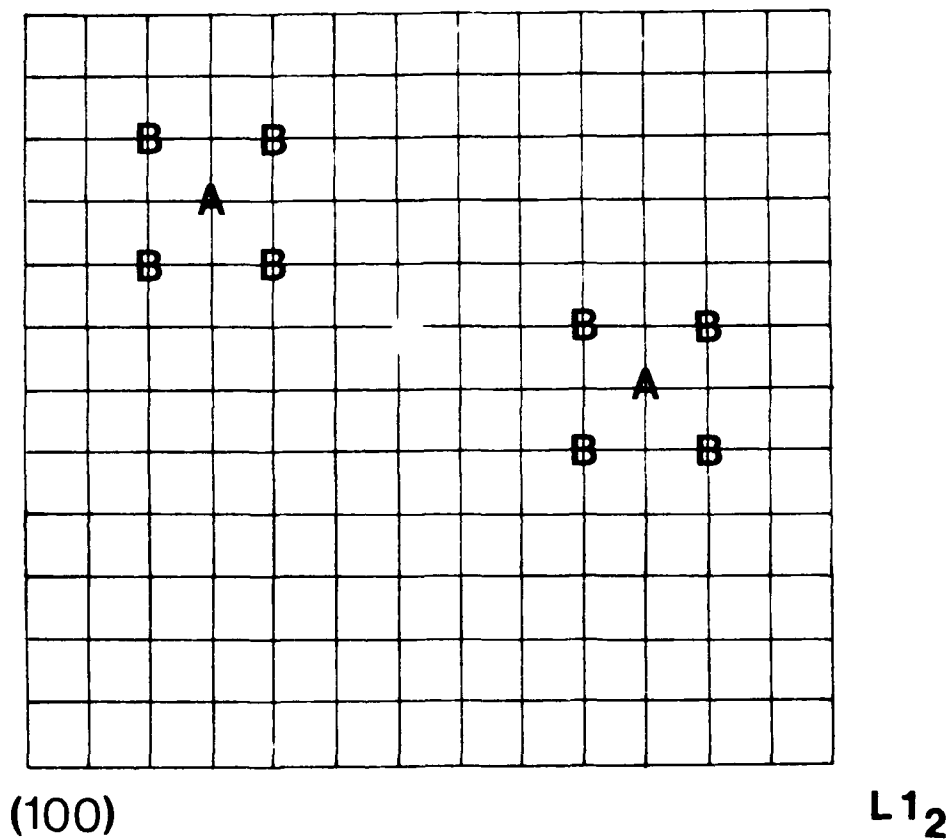


FIGURE I-15. Schematic illustrating the A and B positions on a (100) plane in an L₁₂ structure at two different positions.

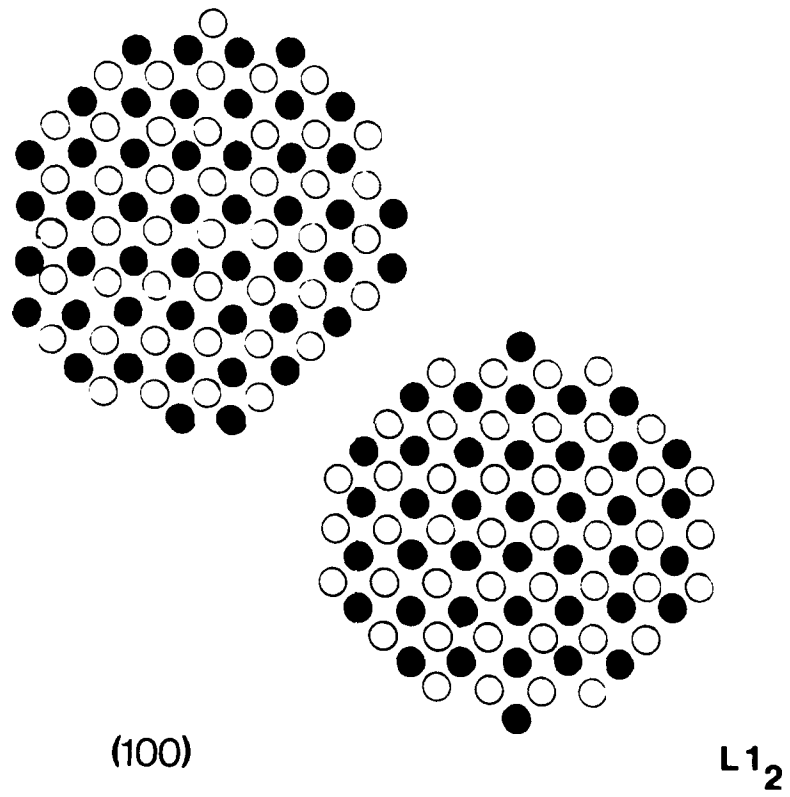


FIGURE I-16. Illustration of two growing δ' precipitates.

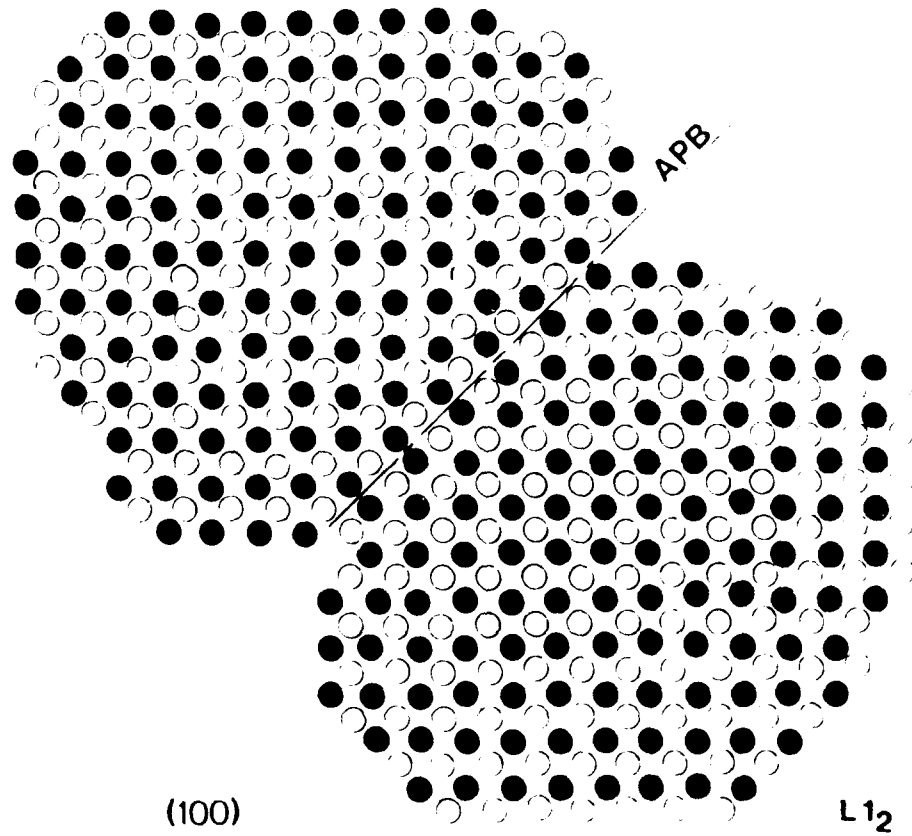


FIGURE I-17. Illustration of particle formed by the encounter of two particles, forming an antiphase domain boundary (APB).

SECTION II. - LIST OF TABLES

- TABLE II-1. The Composition (in weight percent) of the Two Al-Li Alloys.
- TABLE II-2. The Longitudinal Tensile Properties of Al-Li-Mn Sheet Solution Heat Treated at 552°C, Cold Water Quenched and Aged at 200°C
- TABLE II-3. The Longitudinal Tensile Properties of Al-Li-Zr Sheet Solution Heat Treated at 552°C, Cold Water Quenched and Aged at 200°C
- TABLE II-4. Number of δ' Precipitates Examined at 200°C for the Al-2.8Li-0.14Zr Alloy.
- TABLE II-5. Mean Particle Diameter \bar{D} , Median, and Standard Deviation and Coefficient of Variation for Al-2.8Li-0.14Zr Alloy.
- TABLE II-6. The Effect of Aging Time at 200°C on the Mean Particle Diameter, \bar{D} , the Standard Deviation, s , and the Coefficient of Variation, s/\bar{D} , for the Al-Li-Mn Alloy [8].
- TABLE II-7. Experimental Values Determined From the Relationship:
$$\bar{R}^3 - R_{CO}^3 = Kt.$$

SECTION II - LIST OF FIGURES

- FIGURE II-1. Yield strength as a function of isothermal aging time for the two alloys.
- FIGURE II-2. Histogram of the δ' particles in the Al-Li-Zr alloy aged 48 hours at 200°C.
- FIGURE II-3. Histogram of the δ' particles in the Al-Li-Zr alloy aged 1 week at 200°C.
- FIGURE II-4. Histogram of the δ' particles in the Al-Li-Zr alloy aged 2 weeks at 200°C.
- FIGURE II-5. Histogram of the δ' particles in the Al-Li-Mn alloy aged 2 weeks at 200°C.
- FIGURE II-6. Separated histograms of the δ' particles in the Al-Li-Zr alloy aged 48 hours at 200°C.
- FIGURE II-7. Separated histograms of the δ' particles in the Al-Li-Zr alloy aged 1 week at 200°C.
- FIGURE II-8. Separated histograms of the δ' particles in the Al-Li-Zr alloy aged 2 weeks at 200°C.
- FIGURE II-9. The relationship between \bar{R}^3 and isothermal aging time, t , at 200°C for the Al-Li-Mn and Al-Li-Zr alloys.

SECTION II.

THE INFLUENCE OF ZIRCONIUM ON THE COARSENING OF δ' (Al_3Li) IN AN Al-2.7Li-0.14Zr ALLOY

INTRODUCTION

Aluminum alloys containing significant lithium additions have repeatedly demonstrated potential for the development of an alloy with unique and highly desirable combinations of mechanical and physical properties [II-1 - II-4]. Until recently fracture toughness and ductility have been unacceptable for many aerospace applications. However, many of the new alloy systems presented in Reference II-4 show promise.

In addition to containing Li, Mg and Cu all the alloys of commercial interest referenced in [II-4] contain small, intentional additions of an ancillary element. All commercial high strength I/M aluminum alloys contain ancillary element additions which control grain size and degree of recrystallization in wrought products. Traditionally these ancillary element additions have been chromium and manganese although recently some of the new high toughness 7XXX alloys contain zirconium. It should be noted that most of the successful Al-Li alloys reported in References II-2 - II-4 contain zirconium.

When zirconium is added to Al-Li alloys it is very effective in inhibiting recrystallization [II-2]. The small coherent Al_3Zr precipitates retard subgrain boundary migration. Rystad and Ryum [II-5] have suggested that the coherent, oriented nature of the Al_3Zr interface imparts a high drag force to the recrystallization front since the precipitate/matrix interface must change from coherent to semicoherent or incoherent as the recrystallization front passes, or if the orientation relationship between the particle and matrix must be maintained then the particles must dissolve and re-precipitate after the boundary passes through their region; either of these two processes require considerable energy. These explanations are consistent with and have been used to explain [II-2] the experimental observations that the recrystallization temperature of

aluminum alloys containing zirconium tend to be higher than those alloys which contain either chromium or manganese.

There are two other interesting observations which have been made concerning Al-Li-Zr alloys. The first observation is that these alloys tend to age more rapidly than similar alloys which contain manganese, for example, as the ancillary element [II-2,II-6]. The second observation is that Al_3Li precipitates appear to nucleate on the existing Al_3Zr precipitates [II-7] as well as in the matrix.

In a recent publication [II-8] the results of a quantitative transmission electron microscopy (TEM) investigation of the coarsening process of the metastable δ' phase in an Al-Li-Mn was presented. Particle size distributions (PSD's) were determined for a variety of aging times at 168, 200 and 225°C. The growth of the δ' was found to obey Ostwald ripening kinetics. A normal distribution was found to more closely approximate the experimental PSD's rather than the negatively skewed or log-normal distribution predicted by many of the Ostwald ripening theories. Since the rapid aging of Al-Li-Zr alloys has been well documented, a comparative investigation was initiated to determine the mechanism of accelerated coarsening in Al-Li-Zr alloys.

EXPERIMENTAL PROCEDURE

Two Al-Li alloys containing approximately the same lithium content were cast in an ingot 150mm in diameter. One alloy contained manganese and the other zirconium. High purity aluminum was melted in an open hearth furnace and was fluxed with Cl_2 to remove H_2 . The melt was then covered with a molten LiCl-LiF salt mixture and the alloying elements were added. The molten alloy was then transferred to a D.C. casting unit under an inert gas atmosphere which was used to minimize the oxidation of lithium. The chemical compositions of the two alloys are given in Table II-1.

The ingots were preheated in argon for 12 hours at 454°C and then for 13 hours at 516°C. The preheated ingots were reheated to 371°C and were direct extruded into round rods 50.8mm in diameter. The extruded rods were reheated in air for 0.5 hours at 482°C and were hand forged into 1.2cm plates at 200°C. The hand-forged plates were annealed in lead for 5 minutes at 550°C and were quenched in cold water. They were then cold rolled approximately 90% without further annealing. The cold rolled sheet was solution heat treated (SHT) at 552°C in a lead bath then quenched in cold water and artificially aged. To relate the average particle size and the particle size distribution of δ' (Al_3Li) in the Al-Li-Zr alloy to that previously reported in the Al-Li-Mn system [II-8] the Al-Li-Zr alloy was aged for different aging times from 48 hours to 2 weeks at 200°C.

The longitudinal tensile properties were obtained using a sheet-type subsized standard ASTM specimen design. The ultimate tensile strength, the yield strength (0.2% offset) and the elongation were determined.

Microstructures were examined using optical and TEM techniques. The grain morphologies were determined using optical microscopy; the size distribution of δ' and Al_3Zr precipitates in the Al-Li-Zr alloy were determined by TEM. Centered dark field (CDF) images were found to give good contrast between images of the δ' precipitate and the matrix. Particle size measurements were made directly from the TEM negatives using a semi-automatic EyeCom II image analyzing system. The EyeCom II is interfaced with a DEC PDP-11 minicomputer which was programmed to collect, store, and manipulate the raw data.

RESULTS

Mechanical Properties

The longitudinal tensile properties for the two alloys are presented in Tables II-2 and II-3. The yield strength for the two alloys versus artificial aging time are plotted in Figure II-1. Two important features are illustrated by Figure II-1. They are: 1) the time to reach peak strength is more rapid in the Al-Li-Zr compared to a similar Al-Li-Mn alloy, and 2) the Al-Li-Zr alloy overages more rapidly than the corresponding Al-Li-Mn alloy. These two characteristics have been observed in numerous investigations.

Grain Structure

The Al-Li-Mn alloy was fully recrystallized with a grain size of approximately ASTM 5, whereas the Al-Li-Zr alloy was unrecrystallized in the interior of the sheet with a thin recrystallized layer at the surface. The subgrain size as estimated from TEM negatives was approximately $1.0\mu\text{m}$. However, the subgrain structure was generally not uniform and contained areas with very large subgrains.

Distribution and Size of Al_3Zr Precipitates

Since the Al_3Zr particles have a similar morphology to the Al_3Li particles, as-quenched foils were examined to determine the size and distribution of the Al_3Zr particles. TEM revealed the presence of subgrains and the non-uniformly distributed Al_3Zr particles. The average particle diameter of the Al_3Zr was approximately 200A.

Distribution and Size of Al_3Li Precipitates

The δ' precipitates are easy to identify with clear precipitate-matrix interfaces using CDF techniques. However, small dark circles were observed lying inside some of the δ' precipitates. As documented in a recently published paper [II-7], these small interior particles are thought to be Al_3Zr .

By taking a number of TEM micrographs at a particular aging condition and compiling all the measurements, a PSD was constructed. A representative histogram is shown in Figure II-6. For all the aging conditions investigated, the PSD's were asymmetrical having a long tail to the right of the central maximum, a positively skewed distribution. The clear asymmetric nature of the distribution of the PSD's in the Al-Li-Zr alloy is in contrast to the symmetrical distribution found in the Al-Li-Mn alloy having identical composition [II-8]. For comparison, Figure II-3 shows a PSD for a comparable aging treating of the Al-Li-Mn alloy.

Since an asymmetry was present in the PSD's, an attempt was made to determine if the Al_3Zr particles were affecting the shape of the PSD's. PSD's were constructed for each aging condition using the Al_3Li particles that did not contain the Al_3Zr precipitates and those that contained the Al_3Zr precipitates. The number of negatives examined and the number of particles measured for each aging condition are summarized in Table II-2. The aging times 48 hours and 336 hours were replicated.

Examples of the separated PSD'S for several aging conditions are shown in Figures II-4 - II-6. The average particle size, standard deviation and coefficient of variation for each of the PSD's are summarized in Table II-3. For comparison the particle size results [II-8] for the Al-Li-Mn aged at 200°C are presented in Table II-4.

For all the data presented in Tables II-3 and II-4, the cube of the respective mean particle sizes versus aging time are plotted in Figure II-7. A linear analysis of the data

was performed and the results are summarized in Table II-5.

At every aging condition examined, three observations were consistent.

1. Comparison of the experimental results presented in [II-8] for the Al-Li-Mn alloy shows that for similar aging conditions the average particle size of all the δ' particles in the Al-Li-Zr was greater than the average δ' particle size in the Al-Li-Mn alloy. Classifying the δ' particles in the Al-Li-Zr alloy, as shown in Table II-3, indicates that the average particle size of the composite δ' particles is consistently larger than the Al_3Zr -free δ' particles, and furthermore the Al_3Zr -free δ' particles in the Al-Li-Zr alloy were approximately the same size as the δ' particles in the Al-Li-Mn alloy aged under similar conditions.
2. The combined PSD's for δ' in the Al-Li-Zr alloy was asymmetrical, skewed to the right in comparison to the symmetrical PSD's in the Al-Li-Mn having the same lithium content and aging practice. The PSD's for the composite particles were displaced to the right of the Al_3Zr -free δ' PSD's. Consequently, the mean and the median were always greater for the composite particles compared to the Al_3Zr -free δ' particles.
3. The coefficients of variation, that is, the estimate of the standard deviation normalized by the mean ($\frac{S}{D}$) of the PSD's of the composite particles were always smaller than those PSD'S constructed from Al_3Zr -free δ' particles.

DISCUSSION

By comparing the Al-Li-Zr with another alloy having identical lithium content and comparing identical aging conditions it is apparent that zirconium plays a significant role in the development of microstructure and properties in the Al-Li system. Consequently, this discussion will focus on the distribution, precipitation, and interaction of zirconium with microstructure in the Al-Li-Zr system.

In terms of the quantity, zirconium is a minor alloy addition, however, in terms of its influence on the microstructure of a wrought alloy it is a significant addition. The addition of zirconium retards recrystallization and in Al-Li alloys the retained substructure in the wrought product improves strength. As observed in this investigation, the unrecrystallized Al-Li-Zr reached a higher peak strength than did the Al-Li-Mn alloy.

The equilibrium diagram for the aluminum-rich end is of the peritectic type [II-9]. The peritectic temperature is slightly above the melting point of pure aluminum. The limit of solid solubility is 0.28 weight percent, however, from the point of view of casting an alloy containing zirconium, the composition at the break in the liquidus curve (0.11% zirconium) is the composition of interest. Compositions in excess of this value run the risk of containing the coarse primary Al-Zr phase. Compositions up to approximately .18 weight percent Zr can be cast using small book-mold ingots where the solidification rate is relatively rapid. However, for large commercial ingots where the solidification rates are slow, the limits on the zirconium level approach 0.11%.

In comparison to the precipitation hardening elements such as lithium, magnesium and copper for example, zirconium has a relatively low diffusivity and tends to remain in solution after casting. Since the solute distribution coefficient k (C_S/C_L) is slightly greater than 1, the zirconium tends to segregate in the interior of the dendrites rather than in the interdendritic channels where the eutectic elements would be segregated.

During the preheating* cycle, the lithium which is cored homogenizes and goes into solution, whereas the zirconium precipitates out of solution since the solid solubility of Zr is small at the ingot preheating temperatures. The zirconium precipitates from the supersaturated solution where it was located as a result of solidification coring. The result is a non-uniform distribution of Al_3Zr . Consequently, high strength ingot metallurgy alloys containing zirconium tend to have grain structures that are for the most part unrecrystallized, but due to the inhomogeneous distribution of Al_3Zr , regions of coarse recrystallized grains are often observed and the subgrain size distribution also tends to be broad. For example, we observed non-uniform subgrain or grain structures not only at the TEM level of observation but also at the optical level.

Rystad and Ryum [II-5] have shown that in binary Al-Zr alloys decomposition of the supersaturated solid solution during preheat occurs by forming the metastable Al_3Zr phase. This phase exhibits a cubic $L1_2$ structure and thus in the TEM they can easily be imaged by using $\{100\}$ or $\{110\}$ superlattice reflections. As-quenched Al-Li-Zr alloys were examined to determine the size and size distribution of Al_3Zr particles using CDF superlattice reflections for the imaging condition. However, unlike either the binary work of Rystad and Ryum or in the DF images of δ' observed in this study, bright images of the Al_3Zr particles were not produced. The same observation has been described by Gayle and Vander Sande [II-7]. To account for this observation they proposed two possible explanations on the low level of electron scattering of Al_3Zr by the superlattice reflections. One explanation is that the Al_3Zr is a disordered phase when present in the Al-Li system. Alternatively, they proposed that Li is incorporated onto the Zr-sublattice in the Al_3Zr phase and that modifies the atomic scattering factors such that for the composition close to $\text{Al}_3(\text{Li}_{0.6}\text{Zr}_{0.4})$ $F_{001} \approx 0$. Either of these two explanations could account for the lack of a strong DF image. Of the two possible

* A thermal treatment prior to deformation whose primary purpose is to homogenize the ingot and precipitate high-temperature phases.

explanations, the one that tends to be the most reasonable is the substitution of Li on the zirconium sublattice in the $L1_2$ structure. In an alloy development program reported in reference [II-6] from which the alloys used in this investigation were cast, it was reported that the zirconium containing Al-Li alloys had a significantly greater resistance to recrystallization than the Mn containing lithium alloy or for that matter other aluminum alloys containing zirconium. Since Al_3Li and Al_3Zr are isostructural, two possibilities were proposed to explain the effect of the small amount of zirconium on maintaining the unrecrystallized structure through all processing stages, including cold rolling into sheet. The first is that lithium may modify the solubility of zirconium in aluminum, thus producing a higher volume fraction of Al_3Zr . The second possibility is that lithium may substitute for zirconium, thus giving a higher volume fraction of dispersoid. Consequently, in light of the observations in this research along with those of Gayle and Vander Sande [II-7] we propose that some lithium is incorporated in the Al_3Zr precipitates, thus giving a greater effective volume fraction of Al_3Zr to retard the recrystallization process.

Because the Al_3Zr particles in the as-quenched alloy act as surfaces upon which the Al_3Li can precipitate, R_{CO} should not be taken as zero for the onset of coarsening. Therefore, the experimental data were analyzed using the kinetic law, $\bar{R}^3 - R_{CO}^3 = kt$, predicted by the LSW [II-10,II-11] theory rather than the reduced form $R \propto Kt^{1/3}$. Table II-5 summarizes the results of applying the kinetic law to the various types of δ' particles investigated. It is important to note that the extrapolated intercept R_{CO} for the composite particles is much larger than the extrapolated intercept for the Al_3Zr -free δ' particles. This experimentally verifies that the composite particles begin coarsening at larger values than the Al_3Zr -free δ' particles, thus resulting in a bimodal δ' PSD. Furthermore, the difference of the above intercept, $2R_{CO}(III) - 2R_{CO}(II) \approx 200A$, is approximately the average Al_3Zr particle diameter experimentally determined.

A comparison of the rate constants for different kinds of δ' particles shows that the rate constant of δ' particles containing Al_3Zr is significantly higher than the Al_3Zr free δ' particles. According to the LSW theory, particles greater than a critical particle size that is assumed to be equal to the average particle size, are more stable than particles that are less than a critical particle size. Since the composite particles are initially larger than the surrounding Al_3Zr -free δ' particles the composite particles continue to grow at the expense of the smaller δ' particles. The composite particles will continue to grow at a faster rate than the zirconium-free δ' particles as long as there are sufficient numbers of small δ' particles within \sqrt{Dt} of the composite particles to provide the solute. Another important observation that has been made is that the PSD's of the zirconium-free δ' particles have an asymmetric distribution with a tail to the right, a positive coefficient of skewness. Figures II-2 - II-6. The coefficients of skewness for those histograms for the Al_3Zr -free δ' particles were always greater than zero. The particles that supply the solute for the coarsening process are the smaller δ' particles. Consequently, the smaller zirconium-free δ' particles are always unstable and are preferentially dissolving, thus the PSD is truncated at the small particle size end of the distribution.

The more rapid aging response of the Al-Li-Zr alloy compared to the Al-Li-Mn alloy can be explained by comparing the PSD's for the two alloys at similar aging conditions. We might, therefore, predict that the average particle sizes of δ' phase at peak yield strength for both alloys should be the same. The absolute value of yield strength is dependent upon the PSD, the degree of recrystallization and the subgrain structure. During aging the rate of increase in yield strength, however, is due to the change in the particle size distribution. Increasing the mean particle size will increase the yield strength on the underaging side of the yield strength-aging time response curve, and increasing the mean particle size will decrease the yield strength on the overaging side of the yield strength-aging time response curve. As shown in this investigation, the

mean particle size for the Al-Li-Zr alloy is displaced to larger particle sizes compared to the Al-Li-Mn alloy identically aged. Figure II-1 shows that the peak yield strength for the Al-Li-Zr alloy is reached when the alloy is aged at 200°C for 2 hours, and for the Al-Li-Mn alloy is reached after about 50 hours. Using the linear expression of $\bar{R}^3 - R_{CO}^3 = kt$, a calculation of average particle size at peak yield strength for both alloys in their corresponding peak aged conditions shows $\bar{D} \approx 300\text{A}$ would be the critical particle diameter at peak yield strength for both alloys. The initial average particle size for the Al_3Zr particles was approximately $\bar{D} = 200\text{A}$ which is very close to the critical size required for reaching the peak yield strength. Therefore, only a short amount (<5 hours at 200°C) of isothermal aging is necessary for a sufficient number of particles to grow such that the mean size of the entire distribution is in the range of 300A. In other words, the more rapid response to artificial aging of the Al-Li-Zr alloy peak compared to the slower response of the Al-Li-Mn alloy is related to the precipitation of δ' on the pre-existing Al_3Zr particles.

CONCLUSIONS

1. The Al_3Zr particles act as preferential sites for the nucleation and growth of δ' in the Al-Li-Zr system.
2. The PSD of the δ' particles is affected by the presence of the Al_3Zr particles. The distribution is shifted to the right.
3. A separation of the PSD shows a bimodal distribution of δ' .
4. The change in the PSD due to the presence of the Al_3Zr phase accelerates the aging kinetics of the alloy, consequently, the zirconium containing alloy ages more rapidly than a similar alloy not containing zirconium.

REFERENCES

- II-1 T. H. Sanders, Jr. and E. S. Balmuth, *Metal Progress*, 113 (1978), pp. 32-37.
- II-2 E. A. Starke, Jr., T. H. Sanders, Jr., and I. G. Palmer, *J. Metals*, 33 (1981), pp. 24-33.
- II-3 T. H. Sanders, Jr. and E. A. Starke, Jr., ed. *Aluminum-Lithium Alloys* (Proceedings of the First International Aluminum-Lithium Conference, Stone Mountain, GA, May 19-21, 1980), TMS-AIME, Warrendale, PA (1981).
- II-4 E. A. Starke, JR. and T. H. Sanders, Jr., ed. *Aluminum-Lithium Alloys II* (Proceedings of the Second International Aluminum-Lithium Conference, Monterey, CA, April 12-14, 1983), TMS-AIME, Warrendale, PA (1983).
- II-5 S. Rystad and N. Ryum, *Aluminium*, 53 (1977), pp. 193-195.
- II-6 T. H. Sanders, Jr., "Factors Influencing Fracture Toughness and Other Properties of Aluminum-Lithium Alloys," Naval Air Development Center, Contract No. N62269-76-C-0271, Final Report (June 1979).
- II-7 F. W. Gayle and J. B. Vander Sande, *Scripta Metallurgica*, 18 (1984), pp. 473-478.
- II-8 B. P. Gu, J. H. Kulwicki, G. L. Liedl, and T. H. Sanders, Jr., *Materials Science and Engineering*, in press.
- II-9 *Aluminum: Properties and Physical Metallurgy*, ed. John E. Hatch, American Society for Metals (1983), p. 53.
- II-10 I. M. Lifshitz and V. V. Slyozov, *J. Phys. Chem. Solids*, 19 (1961), p. 35.

II-11 C. Wagner, *Z. Electrochem.*, 65 (1961), p. 581.

TABLE II-1.

The composition (in weight percent) of the two Al-Li alloys.

Li	Mn	Zr	Fe	Si	Al
2.78	0.32	-	0.06	0.04	Balance
2.76	-	0.14	0.07	0.04	Balance

TABLE II-2.

Number of δ' Precipitates Examined at
200°C for the Al-2.8Li-0.14Zr Alloy

Aging Time (hours)	Number of TEM Films Examined	Total Number of Precipitates Analyzed
48(I)*	10	1247
48(II)	10	831
48(III)	10	416
R** 48(I)	9	1177
48(II)	9	844
48(III)	9	333
96(I)	6	1322
96(II)	6	941
96(III)	6	381
144(I)	8	1232
144(II)	8	786
144(III)	8	446
168(I)	7	1211
168(II)	7	805
168(III)	7	406
192(I)	7	1140
192(II)	7	750
192(III)	7	390
240(I)	9	1632
240(II)	9	1219
240(III)	9	413
288(I)	7	1357
288(II)	7	1111
288(III)	7	246
336(I)	7	1401
336(II)	7	970
336(III)	7	431
R** 336(I)	9	1359
336(II)	9	1015
336(III)	9	344

- * (I) All δ' particles.
- (II) δ' particles which do not contain Al_3Zr .
- (III) δ' particles which do contain Al_3Zr .
- R** Replicate.

TABLE II-3.
Mean Particle Diameter \bar{D} , Median, and Standard Deviation
and Coefficient of Variation and Coefficient of Skewness for Al-2.8Li-0.14Zr Alloy

Aging Time (hours)	Mean Particle Diameter \bar{D} (A)	Median (A)	Standard Deviation s, (A)	Coefficient* of Variation (CV)	Coefficient** of Skewness
48(I)	372	357	109	0.294	-
48(II)	327	320	82	0.250	0.192
48(III)	483	479	81	0.168	-0.132
***R 48(I)	439	436	131	0.299	-
48(II)	384	378	96	0.249	0.180
48(III)	552	548	120	0.218	-0.220
96(I)	427	411	126	0.295	-
96(II)	407	400	108	0.265	0.136
96(III)	625	617	122	0.195	0.010
144(I)	542	535	168	0.310	-
144(II)	475	468	135	0.283	0.229
144(III)	659	646	169	0.256	0.262
168(I)	544	537	149	0.274	-
168(II)	503	497	132	0.262	0.382
168(III)	624	619	163	0.261	0.440
192(I)	554	548	172	0.310	-
192(II)	507	499	153	0.301	0.113
192(III)	643	632	182	0.289	0.328
240(I)	600	568	178	0.296	-
240(II)	537	524	136	0.253	0.252
240(III)	786	792	179	0.228	-0.432
288(I)	619	609	195	0.315	-
288(II)	565	549	153	0.273	0.504
288(III)	863	861	206	0.238	-0.083
336(I)	633	609	179	0.283	-
336(II)	583	565	153	0.263	0.367
336(III)	782	772	170	0.217	0.137
***R 336(I)	687	680	194	0.283	-
336(II)	632	620	167	0.264	0.209
336(III)	810	803	193	0.238	0.007

* Coefficient of Variation, $CV = \frac{s}{\bar{D}}$

** Coefficient of skewness, C.S. = $\frac{\sum(D_i - \bar{D})^3}{s^3}$.

***R Replicate
(I) All δ' particles.
(II) δ' particles which do not contain Al_3Zr .
(III) δ' particles which do contain Al_3Zr .

TABLE II-4.

The Effect of Aging Time at 200°C on the Mean Particle Diameter, \bar{D} , the Standard Deviation, s , and the Coefficient of Variation, s/\bar{D} , for the Al-Li-Mn Alloy (8).

Aging Time (hours)	\bar{D} (A)	s (A)	Coefficient of Variation $\frac{s}{\bar{D}}$
48	318	83	0.262
96	386	101	0.262
168	483	127	0.263
168*	441	115	0.261
274	482	128	0.266
336	525	145	0.276
672	750	210	0.280
1008	893	240	0.320
1344	910	229	0.252

*Represents duplicate specimen.

TABLE II-5.

Experimental Values Determined From the Relationship:

$$\bar{R}^3 - R_{CO}^3 = Kt$$

\bar{R} : Average particle radius

R_{CO} : Critical particle radius at the onset of coarsening

Alloy	T(°C)	$K \times 10^{-24} \text{ cm}^3/\text{sec}$	R_{CO} (A)
Al-Li-Zr(I)*	200	23.93	195
Al-Li-Zr(II)*	200	20.39	152
Al-Li-Zr(III)*	200	46.38	252
Al-Li-Mn**	200	21.67	-130

* (I) All δ' particles.

* (II) δ' particles which do not contain Al_3Zr .

* (III) δ' particles which do contain Al_3Zr .

** Data from reference (8).

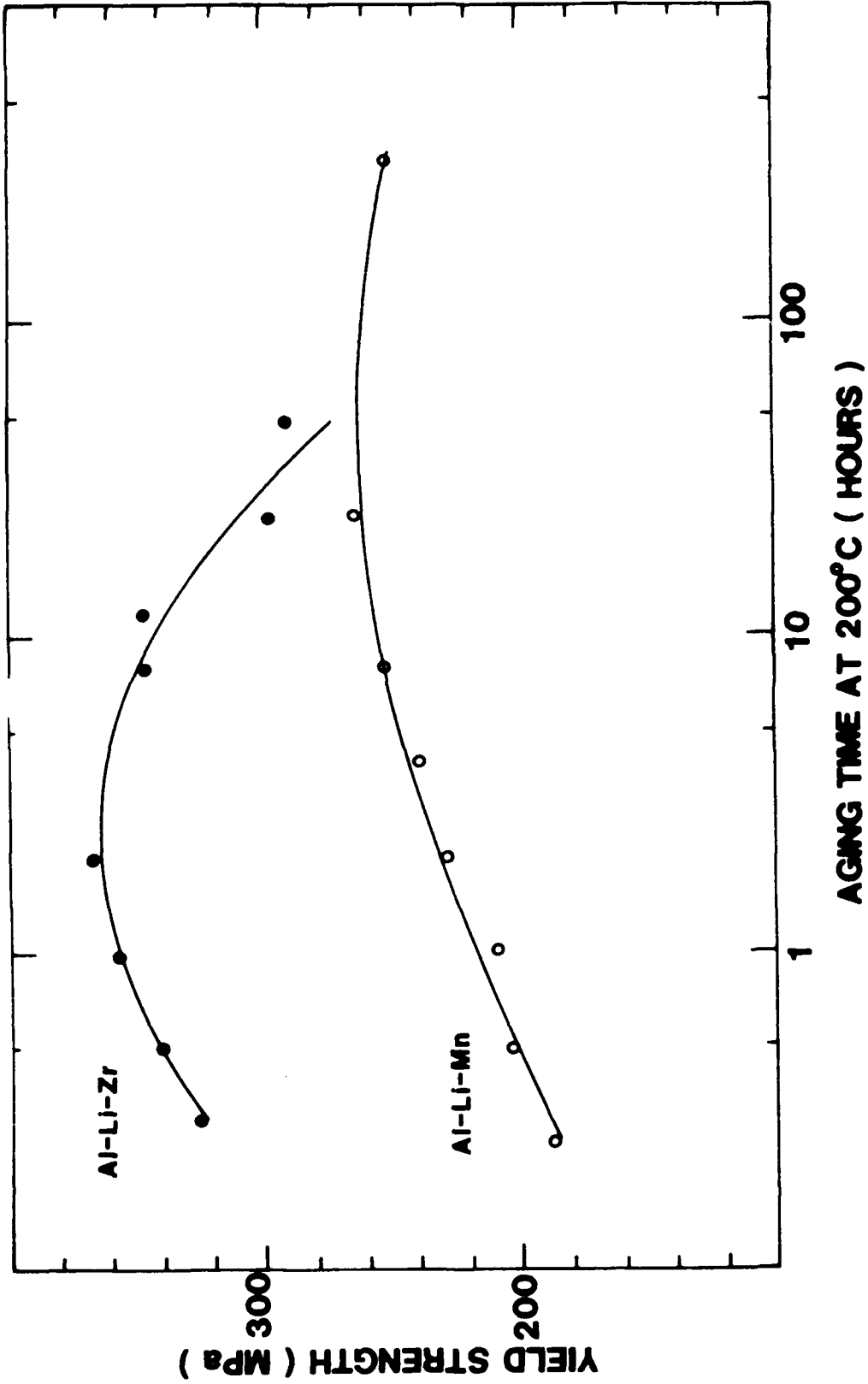


Figure II-1. Yield strength versus aging time for Al-Li-Mn and Al-Li-Zr alloys aged at 200°C.

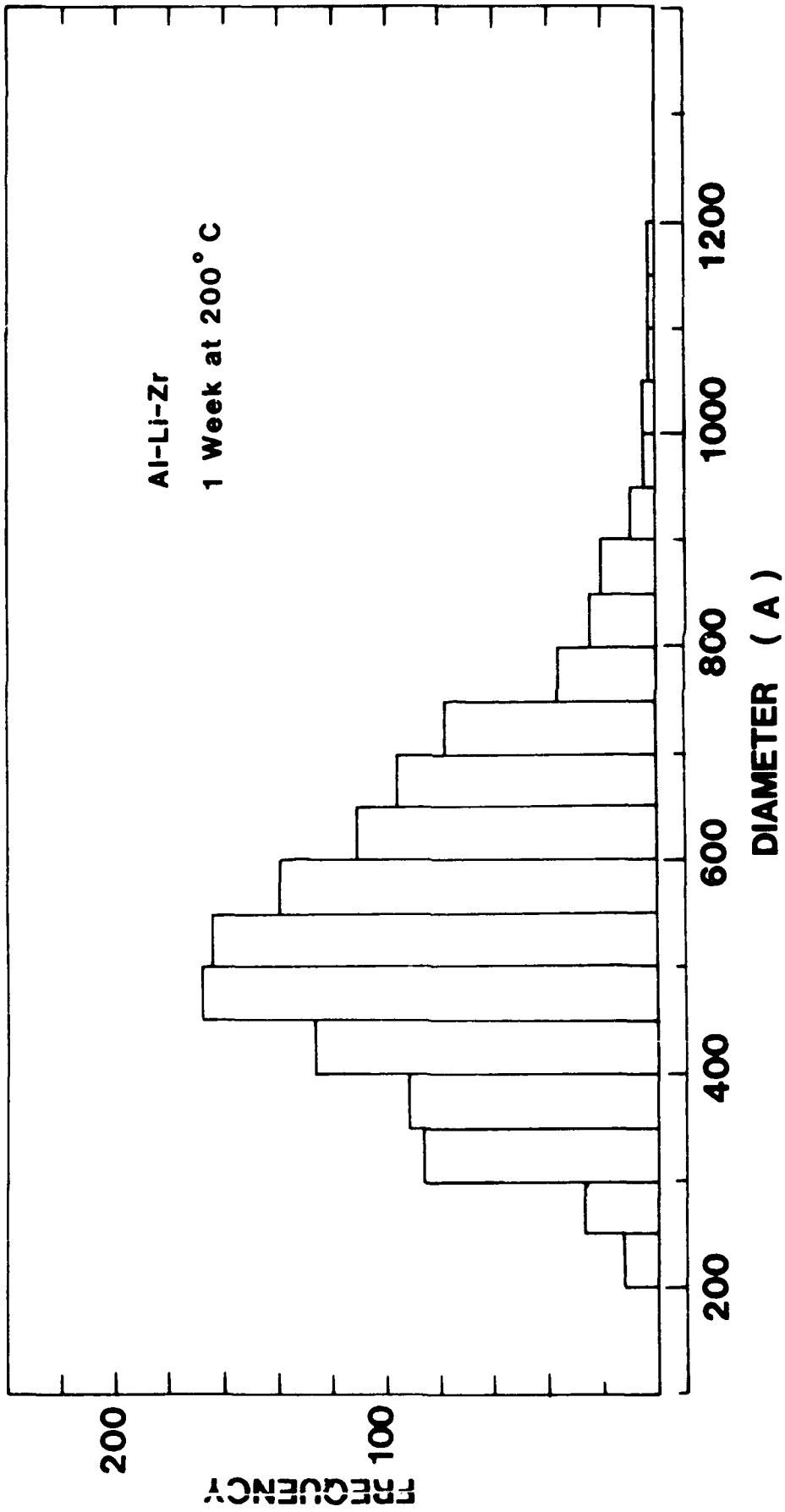


Figure II-2. Histogram of δ' precipitates aged 1 week at 200°C in the Al-Li-Zr alloy.

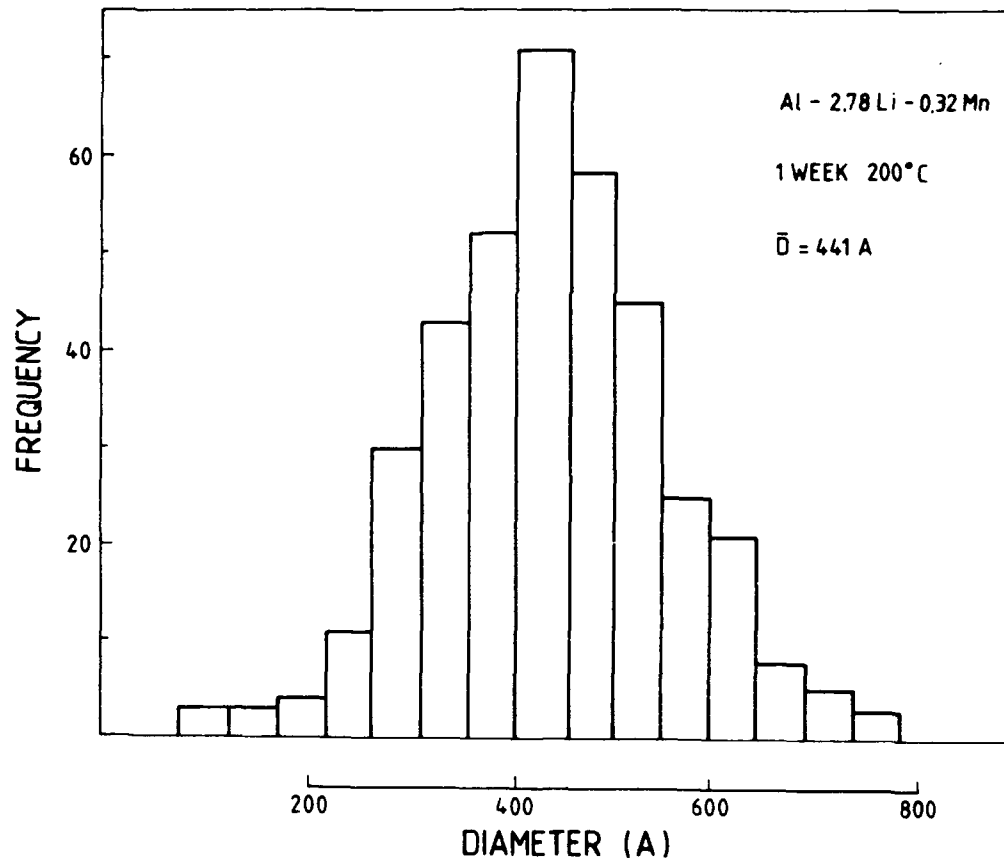


Figure II-3. Histogram of δ' precipitates aged 1 week at 200°C in the Al-Li-Mn alloy.

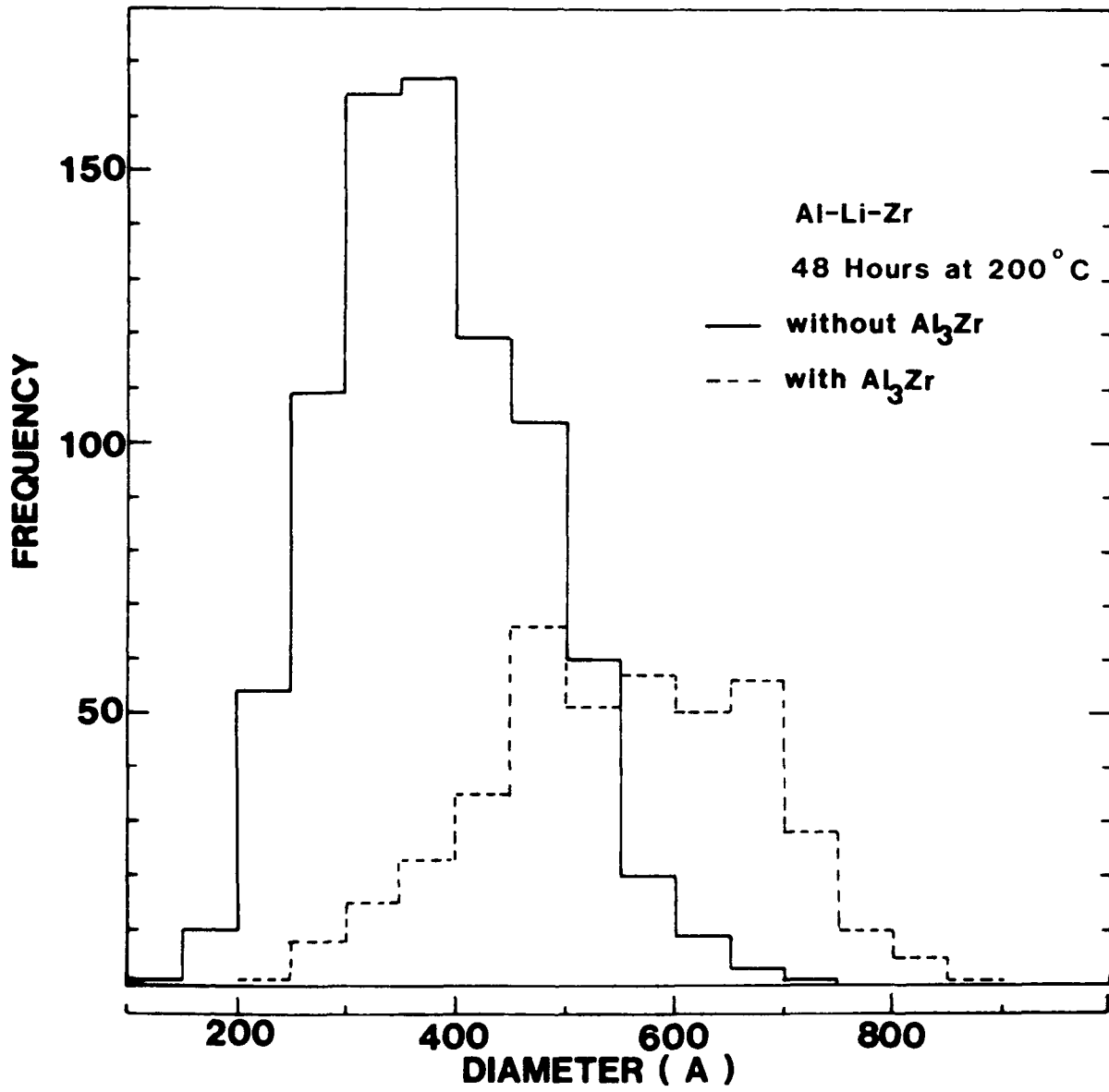


Figure II-4. Separated histogram of δ' precipitates aged 48 hours at 200°C.

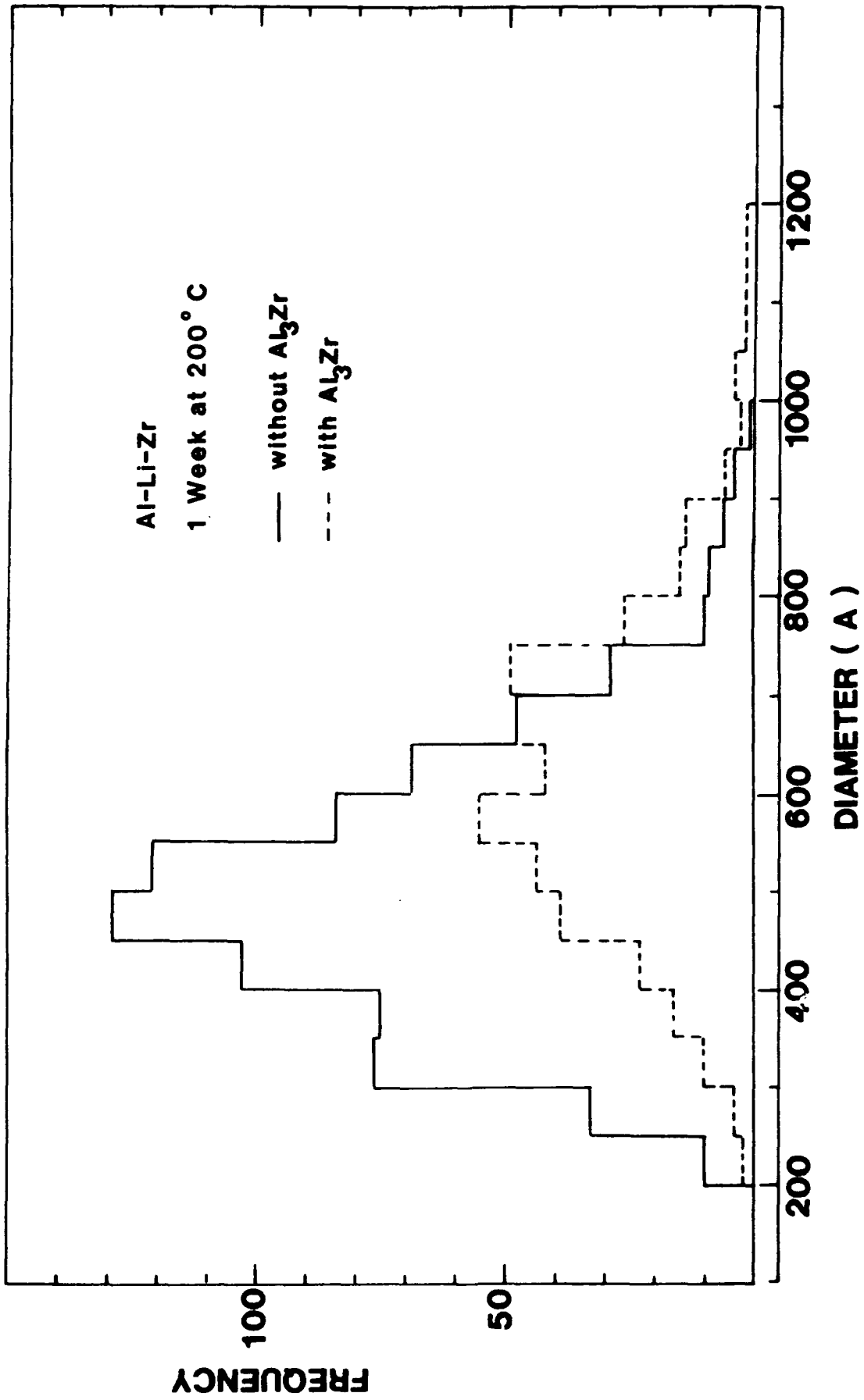


Figure II-5. Separated histogram of δ' precipitates aged 1 week at 200°C.

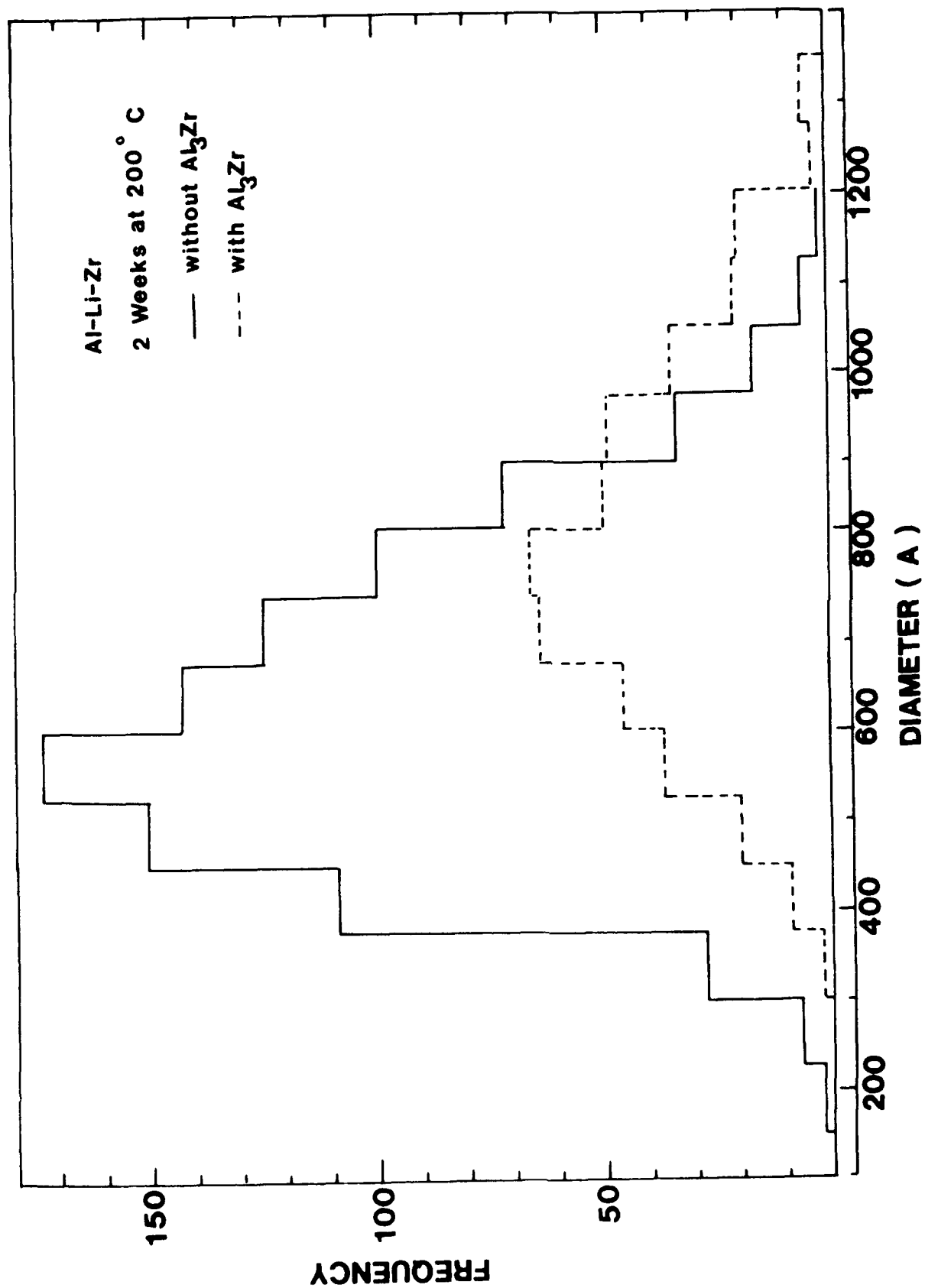


Figure II-6. Separated histogram of δ' precipitates aged 2 weeks at 200°C.

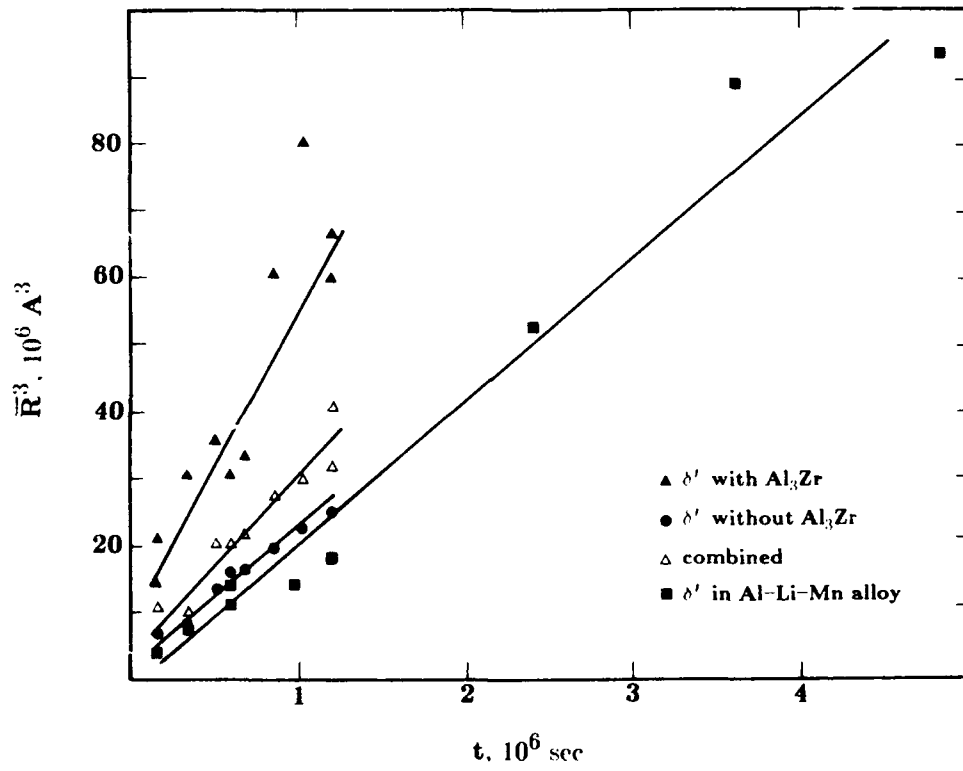


Figure II-7. Linear relation between \bar{R}^3 and time.

SECTION III. - LIST OF TABLES

- TABLE III-1 COMPOSITION OF THE Al-Li ALLOYS
- TABLE III-2 THE EFFECT OF ALLOY COMPOSITION, AGING TEMPERATURE, AND AGING TIME ON THE MEAN PARTICLE DIAMETER, D , MEDIAN, THE STANDARD DEVIATION, s , AND THE COEFFICIENT OF VARIATION, CV , OF THE PSD FOR Al-Li ALLOYS
- TABLE III-3 COEFFICIENT OF SKEWNESS AND COEFFICIENT OF KURTOSIS

SECTION III. - LIST OF FIGURES

- FIGURE III-1. Normalized histogram of the δ' precipitates for Al-2.4Li alloy aged at 200°C for (a) 48 hours and (b) 168 hours.
- FIGURE III-2. Normalized histogram of the δ' precipitates for Al-4.5Li alloy aged at 200°C for (a) 48 hours and (b) 168 hours.
- FIGURE III-3. Generated Weibull distribution curve with parameters (a) $a=1$, and $b=2$, $b=3$, and $b=4$; (b) $b=3.75$, and $a=0.5$, $a=1.0$, and $a=1.5$.

SECTION III.

THE INFLUENCE OF δ' (Al_3Li) LITHIUM CONTENT ON THE KINETICS OF δ' COARSENING AND THE SHAPE OF THE δ' (Al_3Li) PARTICLE SIZE DISTRIBUTIONS (PSD's)

INTRODUCTION

In the investigation presented in the first section of this report the coarsening behavior of δ' in an Al-2.8Li-0.3Mn alloy and showed that the growth of δ' was found to obey Ostwald ripening kinetics. However, the form of the experimental particle size distributions (PSD's) of the δ' was determined to be a distribution which was more symmetrical than the asymmetrical, distribution predicted by many of the Ostwald ripening theories. Consequently, to the expand the body of information on coarsening in general and on δ' in particular, we extended our investigations in Al-Li alloys to include the influence of δ' volume fraction on the coarsening behavior.

EXPERIMENTAL PROCEDURE

A series of aluminum-lithium alloys of compositions described in Table III-1 were cast, hot and cold rolled to a thickness of approximately 2.5 mm. The rolled sheet were sectioned into specimens approximately 1 cm x 1 cm pieces. The samples were solution heat treated (SHT) for 1/2 hour at 600°C in a lead bath and then quenched in cold water.

The samples were aged for different periods of time ranging from 12 hours to 2 weeks at 200 and 225°C. Samples were prepared for transmission electron microscopy (TEM) investigations. Centered dark field (CDF) images were found to give good contrast between images of the δ' precipitates and the matrix. Particle size measurements were made directly from the negatives using a semiautomatic EyeCom II image analyzing system. The EyeCom II is interfaced with a DEC PDP-11 minicomputer

which was programmed to collect, store, and manipulate the raw data.

RESULTS

TEM revealed the presence of the ordered Al_3Li precipitates (δ'). By taking a number of TEM micrographs at a particular aging condition and compiling all the measurements, a PSD was constructed for each aging condition and alloy. The various statistical parameters of the PSD are summarized in Table III-2. Representative PSD's for the 2.4% and 4.5% alloys are shown in Figure III-1 and III-2. It is clear from these figures that the shape of the PSD is a function of alloy content; the more dilute alloy has a long tail on the left side of the distribution, whereas the more concentrated alloy has the long tail on the right side of the distribution.

Alternative to the graphical representation of the data, use was made of two statistical parameters [III-1], the coefficient of skewness, and the coefficient of kurtosis to describe the PSD's.

The skewness is the degree of asymmetry, or the departure from symmetry, of a distribution. For example, if a frequency curve of a distribution has a long tail to the right of the central maximum, the distribution is skewed to the right or is said to have positive skewness. If the reverse is true, the distribution is said to be negatively skewed. The skewness is defined by the relationship

$$\text{skewness} = \frac{\bar{x} - \text{mode}}{s}$$

where \bar{x} is the mean, and s is the standard deviation. Alternatively, one can express the skewness using the third moment about the mean expressed in dimensionless form

is given by the relationship:

$$\text{coefficient of skewness} = \frac{m_3}{s^3},$$

where m_3 is the third moment about the mean. Geometrically, when the coefficient of skewness is > 0 the tail is to the right and when < 0 the tail is to the left.

The other statistical parameter, the coefficient of kurtosis is a measure of the degree of peakedness of a distribution, and is taken relative to a normal distribution. A distribution having a relatively high peak, is called leptokurtic, whereas one which is flat-topped is called platykurtic. The normal distribution which is not very peaked or flat is called mesokurtic.

The coefficient of kurtosis uses the fourth moment about the mean expressed in dimensionless form and is given by the relationship:

$$\text{coefficient} = \frac{m_4}{s^4} - 3,$$

where m_4 is the fourth moment about the mean.

Both of these statistical parameters for the different aging conditions and alloys are summarized in Table III-3.

The coefficient of excess kurtosis was for most cases < 0 indicating that the distribution was flatter than a normal distribution. The coefficient of skewness tended to be < 0 for the dilute alloy, tail to the left of the maximum and > 0 for the concentrated alloy.

PROPOSED RESEARCH

Since the form of the PSD's varied systematically with lithium content, the Weibull statistical distribution function may be used to describe the δ' PSD's. The Weibull distribution has been widely used in the analysis of fatigue failure data, and recently, the Weibull distribution has been used to describe the steady-state particle size distribution which develops during liquid phase sintering [2]. The power of this function lies in the fact that the shape of the distribution can be systematically varied using only two parameters. A general form of the probability density of the Weibull distribution is given by

$$p(x) = \begin{cases} abx^{b-1} \exp(-ax^b) & \text{for } x > 0, a > 0, b > 0 \\ 0 & \text{elsewhere} \end{cases}, \quad (1)$$

and

$$\int_0^{+\infty} p(x) dx = 1 \quad (2)$$

The cumulative probability of the Weibull distribution (or the Weibull distribution function) has the form

$$P(x) = 1 - \exp(-ax^b) \quad (3)$$

The graphs of several probability density curves of the Weibull distribution for a constant value of one of the parameters while varying the other are shown in Figures 3a and 3b. As can be seen in the figures, the value of b tends to affect the symmetry of the distribution and the location of the mean, whereas the value of a primarily affects the location of the mean.

By means of a double-logarithmic transformation, the Weibull distribution can be expressed as

$$\ln \ln \frac{1}{[1 - P(x)]} = \ln a + b \ln x \quad (4)$$

The values of a and b can thus be determined by the linear regression analysis. Since the shape of the Weibull distribution curve can be altered from a negatively skewed to a positively skewed distribution by adjusting the variables a and b , the Weibull distribution function is suitably tailored to approximate the δ' PSD's in binary Al-Li alloys. Therefore, during the next contract we will analyze the PSD's using the Weibull distribution.

REFERENCES

- III-1. M. R. Spiegel, *Statistics, in Schaum's Outline Series in Mathematics*, McGraw-Hill Co., New York, pp. 89-98 (1961).
- III-2. S. Takajo, W. A. Kaysser and G. Petzow, *Acta Metallurgica*, Vol. 32, No. 1, pp. 107-113 (1984).

TABLE III-1 COMPOSITION OF THE Al-Li ALLOYS

Alloy	Density	Li at.%	Li wt.%	Al
1	2.527	8.64	2.37	Balance
2	2.486	10.70	2.99	Balance
3	2.479	11.05	3.10	Balance
4	2.419	14.05	4.04	Balance
5	2.389	15.55	4.52	Balance

TABLE III-2 THE EFFECT OF ALLOY COMPOSITION, AGING TEMPERATURE, AND AGING TIME ON THE MEAN PARTICLE DIAMETER, D, MEDIAN, THE STANDARD DEVIATION, s, AND THE COEFFICIENT OF VARIATION, CV, OF THE PSD FOR Al-Li ALLOYS

Alloy	Aging Temp. (°C)	Aging Time	D (A)	Median (A)	s (A)	CV
Alloy 1	200	48 hrs.	337	340	81	0.241
	200	72 hrs.	386	393	90	0.233
	200	96 hrs.	405	413	96	0.237
	200	168 hrs.	491	500	114	0.232
	225	12 hrs.	400	405	90	0.225
	225	24 hrs.	486	492	112	0.230
	225	48 hrs.	615	621	143	0.233
	225	72 hrs.	662	672	164	0.248
Alloy 2	200	48 hrs.	367	368	89	0.243
	200	72 hrs.	460	457	117	0.254
	200	96 hrs.	525	535	120	0.229
	200	1 week	569	578	136	0.239
	200	10 days	654	646	165	0.252
	225	12 hrs.	461	465	119	0.260
	225	48 hrs.	751	750	191	0.254
	225	72 hrs.	693	701	181	0.261
	225	96 hrs.	800	797	214	0.267
Alloy 3	200	48 hrs.	378	382	95	0.251
	200	72 hrs.	466	476	123	0.264
	200	96 hrs.	546	549	120	0.220
	200	1 week	618	621	139	0.225
	200	10 days	689	696	159	0.231
	225	12 hrs.	439	448	111	0.254
	225	24 hrs.	598	611	164	0.275
	225	48 hrs.	689	696	189	0.274
	225	72 hrs.	724	725	192	0.265
	Alloy 4	200	48 hrs.	432	404	151
200		72 hrs.	482	470	145	0.301
200		96 hrs.	551	542	154	0.279
200		1 week	636	636	181	0.285
200		10 days	729	723	209	0.287
225		12 hrs.	483	470	149	0.308
225		24 hrs.	758	748	244	0.323
225		48 hrs.	969	988	274	0.282
225		72 hrs.	960	961	262	0.272
225		96 hrs.	952	932	261	0.274

TABLE III-2 Continued

Alloy	Aging Temp. (°C)	Aging Time	D (A)	Median (A)	s (A)	CV
Alloy 4*	225	12 hrs.	558	545	154	0.277
	225	18 hrs.	678	662	189	0.279
	225	24 hrs.	706	705	195	0.277
	225	36 hrs.	858	853	264	0.308
	225	48 hrs.	900	880	258	0.287
	225	60 hrs.	962	952	277	0.287
	225	72 hrs.	998	1001	314	0.315
	225	84 hrs.	1071	1075	323	0.301
	225	144 hrs.	1085	1058	288	0.265
Alloy 5	200	48 hrs.	493	483	144	0.292
	200	72 hrs.	541	531	169	0.312
	200	96 hrs.	574	571	164	0.286
	200	1 week	741	735	221	0.298
	200	10 days	810	788	236	0.291
	225	12 hrs.	719	708	233	0.324
	225	24 hrs.	906	872	306	0.338
	225	48 hrs.	1080	1063	361	0.334
	225	60 hrs.	1095	1071	301	0.275
	225	72 hrs.	1104	1061	404	0.366
	225	84 hrs.	1197	1193	322	0.269
	225	96 hrs.	1222	1216	357	0.292
	LSW Predicted Value			0.215		

* replicate

CV: coefficient of variation = s/D

TABLE III-3 COEFFICIENT OF SKEWNESS AND
COEFFICIENT OF KURTOSIS

Specimen No.	% Li	Aging Temp.	Aging Time	Coeff. of Skewness	Coeff. of Kurtosis
1	2.4	200	48 hrs.	-0.3537	-0.5665
			72 hrs.	-0.2355	-0.5799
			96 hrs.	-0.4105	-0.2947
			1 week	-0.4068	-0.3105
2	3.0	200	48 hrs.	-0.3858	-0.4196
			72 hrs.	-0.1052	-0.2176
			96 hrs.	-0.2070	-0.2211
			1 week	-0.2836	-0.2774
			10 days	-0.1666	0.0260
3	3.1	200	48 hrs.	-0.2235	0.0407
			72 hrs.	-0.3299	-0.1607
			96 hrs.	-0.2871	-0.4940
			1 week	-0.4273	-0.2476
			10 days	-0.3677	-0.2777
4	4.0	200	48 hrs.	0.2698	-0.9692
			72 hrs.	0.3192	-0.1839
			96 hrs.	0.2701	-0.2355
			1 week	-0.0534	-0.2356
			10 days	0.1057	-0.3833
5	4.5	200	48 hrs.	0.2017	-0.2591
			72 hrs.	0.2572	-0.1905
			96 hrs.	0.0771	-0.1265
			1 week	0.0075	-0.4723
			10 days	0.1765	-0.2929
1	2.4	225	12 hrs.	-0.4702	-0.0993
			24 hrs.	-0.3358	-0.5289
			48 hrs.	-0.4398	-0.1214
			72 hrs.	-0.3047	-0.8057
2	3.0	225	12 hrs.	-0.3741	-0.4574
			48 hrs.	-0.2639	-0.4162
			72 hrs.	-0.2916	-0.5094
			96 hrs.	-0.1227	-0.4901
3	3.1	225	12 hrs.	-0.3788	-0.4263
			24 hrs.	-0.3540	-0.3666
			48 hrs.	-0.1782	-0.6279
			72 hrs.	-0.2295	-0.2182

TABLE III-3 Continued

Specimen No.	% Li	Aging Temp.	Aging Time	Coeff. of Skewness	Coeff. of Kurtosis
4	4.0	225	12 hrs.	0.0809	-0.4574
4*	"	"	"	0.0760	-0.6081
4*	"	"	18 hrs.	0.2049	0.0009
4	"	"	24 hrs.	0.0674	-0.6241
4*	"	"	"	0.2633	0.4263
4*	"	"	36 hrs.	0.1205	-0.0974
4	"	"	48 hrs.	-0.0534	0.0040
4*	"	"	"	0.3297	0.1902
4*	"	"	60 hrs.	0.0451	-0.0764
4	"	"	72 hrs.	-0.0324	-0.0942
4*	"	"	"	0.0622	-0.9025
4*	"	"	84 hrs.	0.1283	-0.3969
4	"	"	96 hrs.	-0.0322	-0.4177
4*	"	"	144 hrs.	0.0541	-0.5364
5	4.5	225	12 hrs.	0.2770	-0.5948
	"	"	24 hrs.	-0.0896	-1.3003
	"	"	48 hrs.	0.0596	-1.1035
	"	"	60 hrs.	0.1067	-0.3642
	"	"	72 hrs.	-0.1007	-1.5862
	"	"	84 hrs.	0.0450	-0.3575
	"	"	96 hrs.	-0.0653	-0.1895
			LSE Predicted Value	-0.9200	

* Replicate

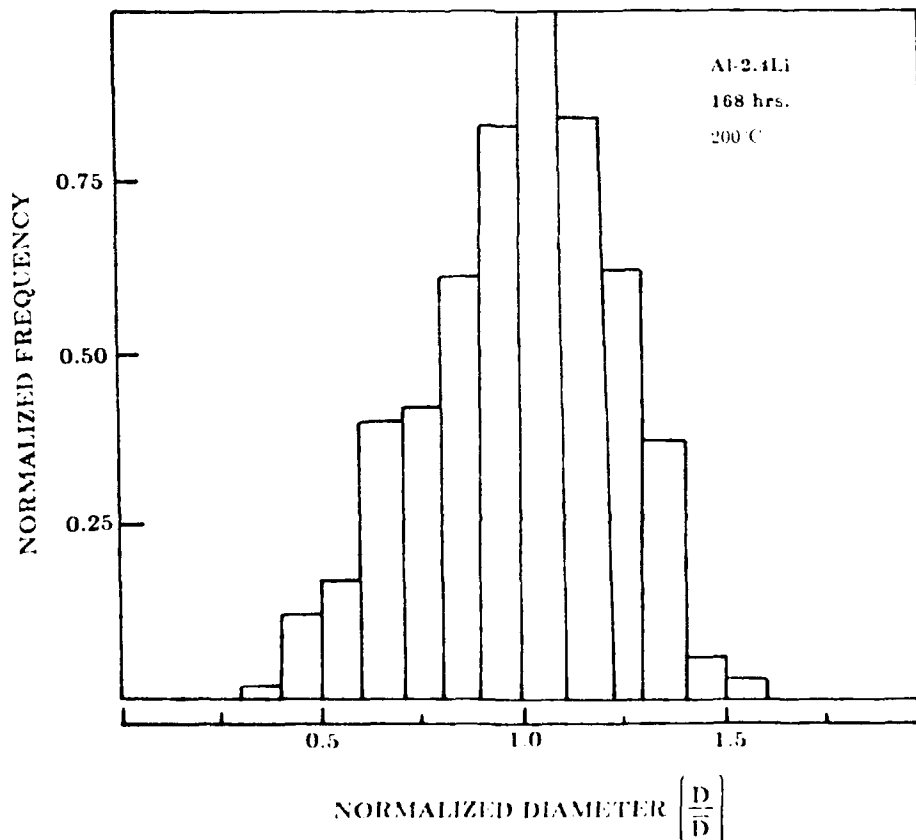
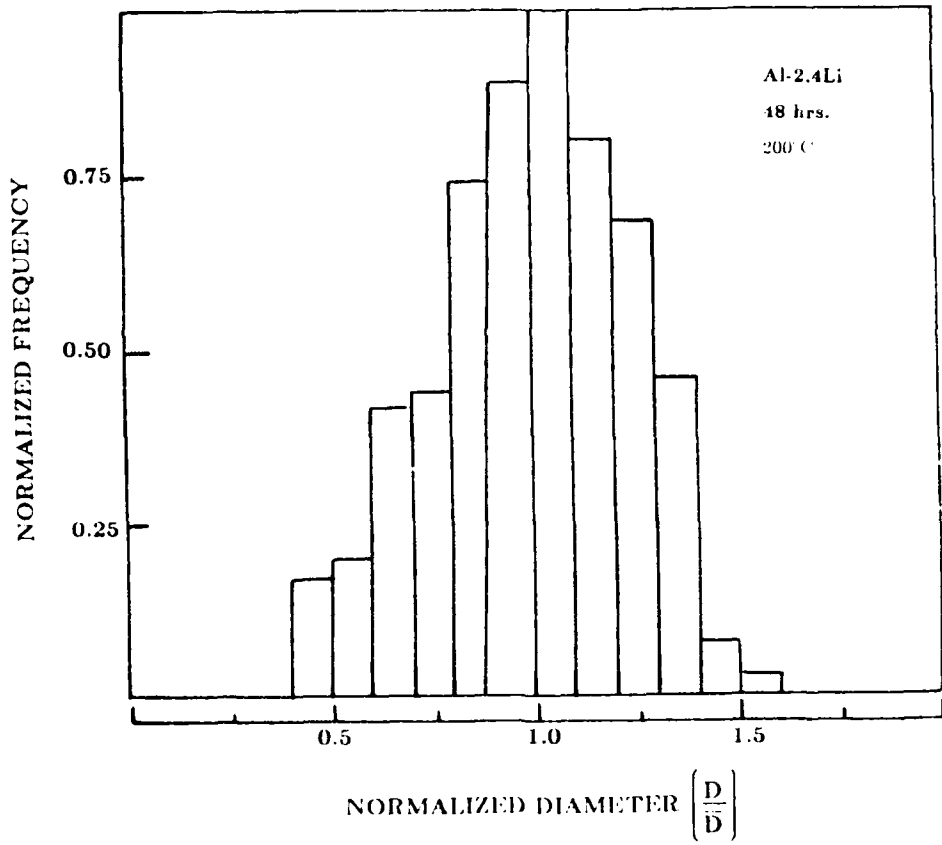


FIGURE 1. Normalized histogram of the δ' precipitates for Al-2.4Li alloy aged at 200°C for (a) 48 hours and (b) 168 hours.

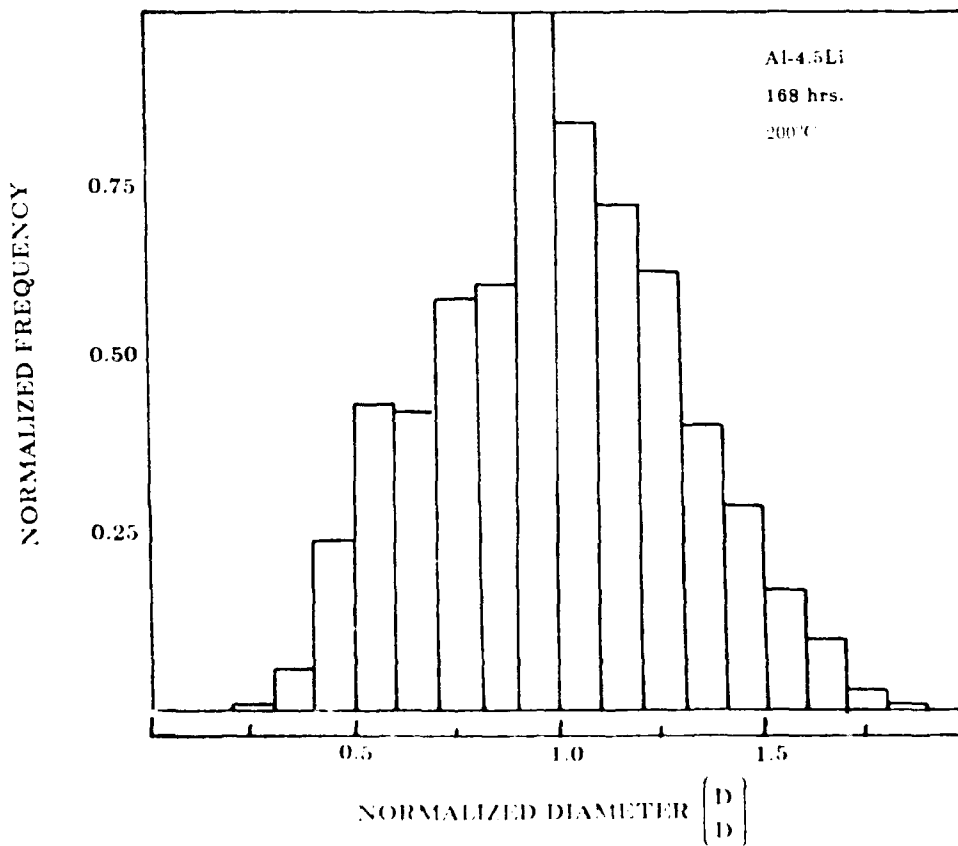
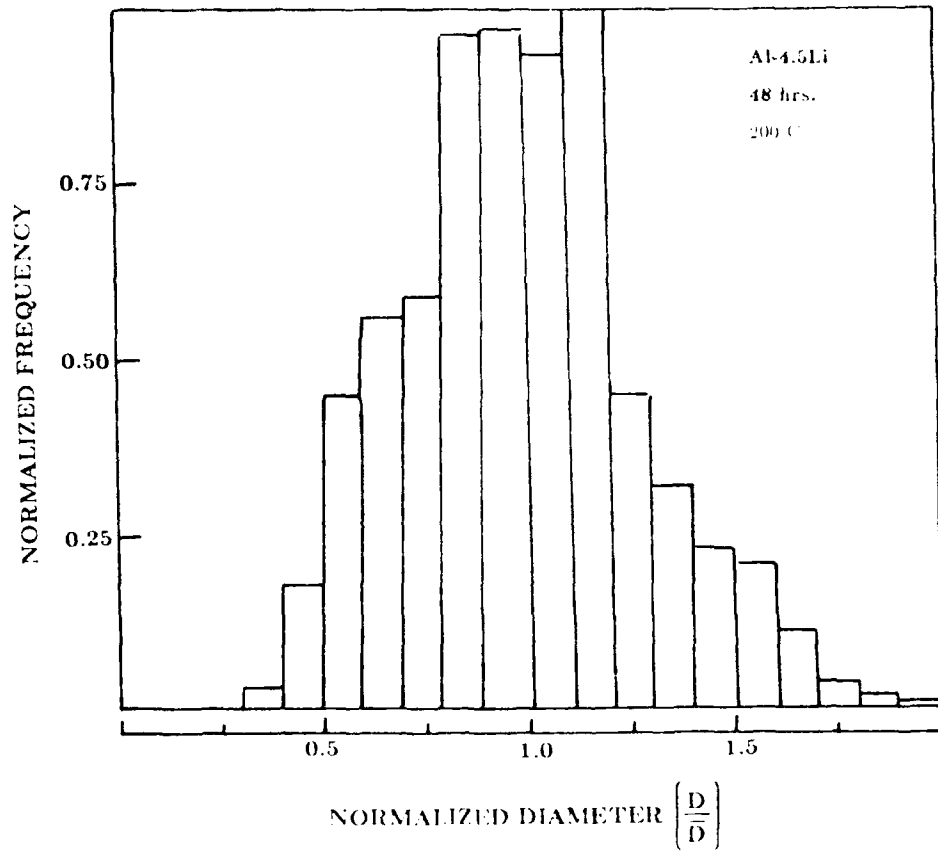


FIGURE 2. Normalized histogram of the δ' precipitates for Al-4.5Li alloy aged at 200°C for (a) 48 hours and (b) 168 hours.

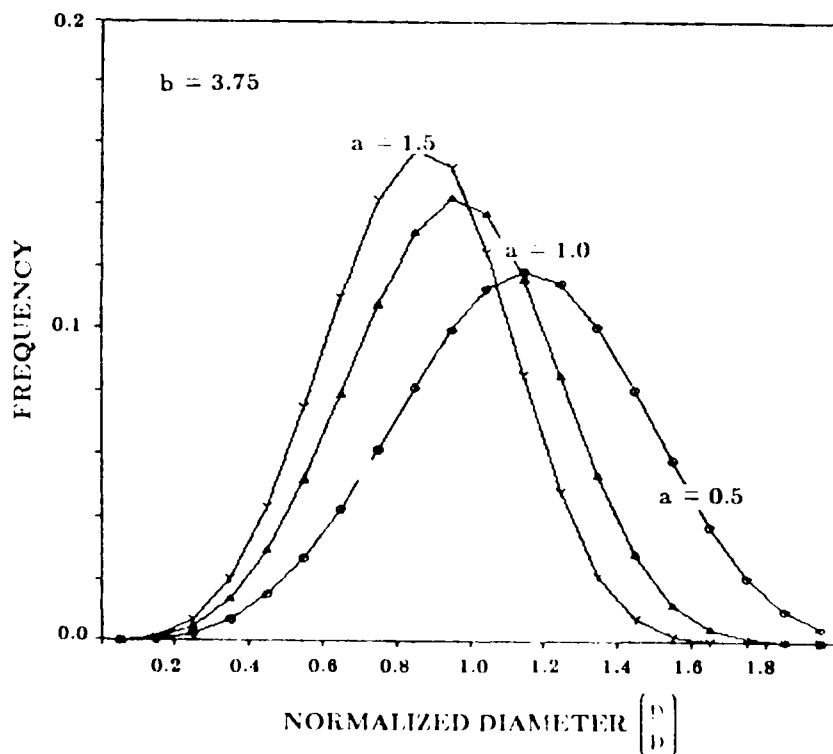
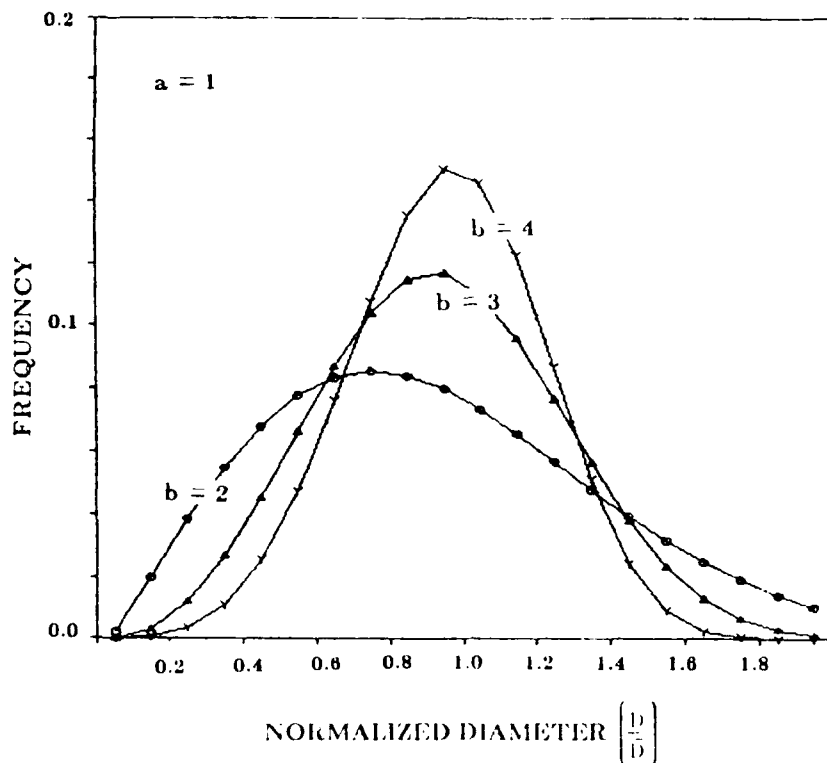


FIGURE 3. Generated Weibull distribution curve with parameters (a) $a=1$, and $b=2, b=3$, and $b=4$; (b) $b=3.75$, and $a=0.5, a=1.0$, and $a=1.5$.

SECTION IV. - LIST OF TABLES

TABLE IV-1. Measured Densities for the Various Al-Li-Cu-Mg Alloys

SECTION IV.
PRELIMINARY DIFFERENTIAL SCANNING CALORIMETRY (DSC)
RESULTS IN THE Al-Cu-Mg-Li SYSTEM

INTRODUCTION

The melting reactions and precipitation reactions which include information on the temperatures, compositions and the phases are important not only academically but are also of importance commercially. Detailed information about the stable and metastable diagrams in the Al-Li-Cu-Mg system is not available. The purpose of this study is, therefore, directed toward supplying some of this needed information.

RESULTS

The results of density and differential scanning calorimetry (DSC) measurements are summarized in Table IV-1. On that table T_E refers to a possible eutectic reaction, T_S a solidus reaction, and T_M a liquidus reaction.

PROPOSED RESEARCH

During the next contract period we will continue the calorimetry studies.

TABLE IV-1.

Measured Densities for the Various Al-Li-Cu-Mg Alloys.

ALLOY	Cu (weight percent)	Mg (weight percent)	Li (weight percent)	Density (gm/cc)	T _E °C	T _S °C	T _M °C
101	1.3	.8	.7	2.874		613	
102	1.3	.5	1.0	2.721		614	
103	1.3	.3	1.3	2.804		620	
104	3.7	.3	1.3				
105	3.5	1.0	1.9	2.688	538		
106	2.4	.5	2.1	2.883	531		
107	2.8	1.7	1.9	2.597	540		
108	2.7	1.4	2.5	2.583	545		
109	2.5	.9	2.6	2.588	548		
110	2.8	.5	2.5	2.589	549		
111	2.3	1.8	2.4	2.566	544		
112	2.2	1.3	2.3	2.630	550		
113A	0.6	2.4	2.7	2.663	542		
113B	0.9	2.4	2.6	2.574	--		
114	2.3	.5	2.2	2.590	547		
115A	2.1	1.3	3.5	2.552	560		
115B	1.9	1.6	3.4	2.576	--		
116	1.7	1.1	3.1	2.569	556		
117	2.3	0.5	3.0	2.600	560		
118	1.6	2.3	2.5	2.549	545		
119	1.9	1.7	2.4	2.550	547		
120	1.8	1.4	2.4	2.560	549		
121	1.8	1.0	2.5	2.564	550		
122	1.8	0.5	2.4	2.631	551		
123	1.8	1.4	3.0	2.688	556		
124	1.7	1.0	3.1	2.593	558		
125	1.7	0.6	3.2	2.661	558		
126	1.4	1.8	1.9	2.633	538		
127	1.5	1.4	2.5	2.558	547		
128	1.4	1.0	2.5	2.618	550		
129	1.3	0.6	2.5	2.567	548		
130	1.4	1.4	3.0	2.597	550		
131	1.3	1.1	3.3	2.662	556		
132	1.3	0.6	3.4	2.693	560		
134	0.9	1.9	2.4	2.554	544		
135	0.9	1.5	2.4	2.620	546		
136	0.9	1.1	2.8	2.565		601	
137	0.8	0.6	2.5	2.714		617	
138	0.9	1.4	3.0	2.520	552		
139	0.9	1.0	3.1	2.516		604	
140	0.7	0.7	2.9	2.555		599	
141	0.5	2.2	2.3	2.636		578	
142	0.5	1.8	2.5	2.518		587	
143	0.5	0.7	2.5	2.568		581	
144	0.5	0.5	2.4	2.563		624	
145	0.4	1.9	3.0	2.509		575	640
146	0.5	1.0	3.1	2.517		599	641
147	0.4	0.6	3.3	2.546		612	649

DISTRIBUTION LIST

Mrs. Gayle Weaver
AIR-5163C4
Naval Air Systems Command
Washington, DC 20361
(5)

Richard Schmidt
Code 310A
Naval Air Systems Command
Washington, DC 20361
(2)

A. P. Divecha
R32
Naval Surface Weapons Center
White Oak, Laboratory
Silver Spring, MD 20910
(3)

Commander
Naval Air Development Center
(Code 606)
Warminster, PA 18974

Naval Sea Systems Command
(Code 03423)
Department of the Navy
Washington, DC 20360

Naval Ships Research &
Development Center
(Code 2812)
Annapolis, MD 21402

Commander
Naval Surface Weapons Center
(Metallurgy Division Code R-30)
White Oak, Laboratory
Silver Spring, MD 20910

Director
Naval Research Laboratory
(Codes: 6380, 6490, 6601, 8430)
(1 each)
Washington, DC 20390

Office of Naval Research
The Metallurgy Program
Code 431
Arlington, VA 22217

Dr. T. R. McNelley
Dept. of Mechanical Engineering
(Code 59)
Naval Postgraduate School
Monterey, CA 93940

Commander
Naval Air Systems Command
AIR-954 (2 copies)
DDC (12 copies)
Washington, DC 20361

Dr. Bruce A. MacDonald
Office of Naval Research
800 N. Quincy Street
Code 431
Arlington, VA 22317

Naval Surface Weapons Center
Library - X211
White Oak, Laboratory
Silver Spring, MD 20910
(3)

Wright-Patterson Air Force Base
Ohio 45433
ATTN: C.L. Harmsworth
AFWAL/MLXE

Wright-Patterson Air Force Base
Ohio 45433
ATTN: W. Griffith
AFML/LLS

AFOSR/NE
Bolling Air Force Base
Washington, DC 20332
ATTN: Dr. A. H. Rosenstein

U. S. Army Armament R&D Command
(ARRADCOM)
Dover, NJ 07801
DRDAR-SCM-P, Bldg. 3409

Metallurgy & Materials Science Div.
U. S. Army Research Office
P.O. Box 12211
Research Triangle Park, NC 27709
ATTN: Dr. G. Meyer

Metallurgy & Materials Science Div.
U. S. Army Research Office
P.O. Box 12211
Research Triangle Park, MD 27709
ATTN: Dr. Phillip Parrish

Commanding Officer
Office of Ordnance Research
Box CM, Duke Station
Durham, NC 27706

Army Materials & Mechanics Research Cnt.
Watertown, MA 02172
ATTN: Dr. A. Gorum

M. H. Brennecke
EH 23
Bldg. 4612
NASA
Marshall Space Flight Center
Huntsville, AL 35812

National Aeronautics & Space Admn.
George C. Marshall Space Flight Center
Huntsville, AL 35812
ATTN: Mr. J. G. Williamson
S&E-ASTN-MMC

National Aeronautics & Space Admn.
Langley Research Center
Materials Division, Langley Station
Hampton, VA 23365
ATTN: Mr. H. F. Hardrath
Stop 188M

National Aeronautics & Space Admn.
(Code RWM)
600 Independence Avenue, SW
Washington, DC 20546

National Aeronautics & Space Admn.
George C. Marshall Space Flight Center
Huntsville, AL 35812
ATTN: Mr. J. G. Williamson
S&E-ASTN-MMC

National Academy of Sciences
Materials Advisory Board
Washington, DC 20418
ATTN: Dr. J. Lane

Director
National Bureau of Standards
Washington, DC 20234
ATTN: Dr. E. Passaglia

ERDA Division of Reactor Development
and Technology
Washington, DC 20545
ATTN: Mr. J. M. Simmons, Chief
Metallurgy Section

AiResearch Manufacturing Co. of America
Sky Harbor Aircraft
402 S. 36th Street
Phoenix, AR 85034
ATTN: Mr. Jack D. Tree
Dept. 93-35-5M

Information Department
Bldg. D
Alcoa Technical Center
Alcoa Center, PA 15069
(3)

W. S. Cebulak
Bldg. B
Alcoa Technical Center
Alcoa Center, PA 15069

J. T. Staley
Alloy Technology Division
Bldg. C
Alcoa Technical Center
Alcoa Center, PA 15069

A. K. Vasudevan
Alloy Technology Division
Bldg. C
Alcoa Technical Center
Alcoa Center, PA 15069

Detroit Diesel Allison Division
General Motors Corporation
Materials Laboratories
Indianapolis, IN 46206

Lycoming Division
AVCO Corporation
Stratford, CT 06497
ATTN: Mr. Barry Goldblatt

Avco Space Systems Division
Lowell Industrial Park
Lowell, MA 01851

Battelle Memorial Institute
505 King Avenue
Columbus, OH 43201
ATTN: Mr. Stephan A. Rubin, Mgr.
Information Operations

D. P. Hill
Physical Metallurgy Section
Battelle, Columbus Lab.
Battelle Memorial Institute
505 King Avenue
Columbus, OH 43201

D. N. Williams
Physical Metallurgy Section
Battelle, Columbus Lab.
Battelle Memorial Institute
505 King Avenue
Columbus, OH 43201

The Boeing Company
Commercial Airplane
ORG. 6-8733, MS77-18
P. O. Box 3707
Seattle, WA 98124
ATTN: Cecil E. Parsons

The Boeing Company
Commercial Airplane
ORG. 6-8733, MS77-18
P.O. Box 3707
Seattle, WA 98124
ATTN: A. Lew Wingert

The Boeing Company
Commercial Airplane
ORG. 6-8733, MS7-18
P.O. Box 3707
Seattle, WA 98124
ATTN: Bill Quist

Mr. W. Spurr
The Boeing Company
12842 72nd Avenue, NE
Kirkland, WA 98033

Dr. W. C. Setzer, Director
Metallurgy & Surface Technology
Consolidated Aluminum Corp.
P. O. Box 14448
St. Louis, MO 63178

The Dow Metal Products Company
Hopkins Building
Midland, MI 48640

General Dynamics
Fort Worth Division
MZ 5984
P.O. Box 748
Fort Worth, TX 76101
ATTN: Mr. E. S. Balmuth

General Dynamics Corp.
Convair Aerospace Division
Fort Worth Operation
P. O. Box 748
Fort Worth, TX 76101
ATTN: Tom Coyle

General Dynamics Convair Div.
P. O. Box 80847
San Diego, CA 92138
ATTN: Mr. Jack Christian
Code 643-10

General Electric Co.
Corporate Research and Development
Bldg. 36-441
Schenectady, NY 12345
ATTN: Dr. J. H. Westbrook, Mgr.
Materials Information Service

General Electric Company
Corporate Research and Development
P. O. Box 8
Schenectady, NY 12301
ATTN: Dr. D. Wood

General Electric Company
Aircraft Engine Group
Material & Processes Technology Lab.
Evendale, OH 45215

General Electric
Missile & Space Division
Materials Science Section
P.O. Box 8555
Philadelphia, PA 91901
ATTN: Technical Library

Dr. Philip N. Adler
Research & Development Center
Grumman Aerospace Corp.
Bethpage, NY 11714

Dr. John M. Papazian
Research Department
Grumman Aerospace Corp.
Bethpage, NY 11714

IIT Research Institute
Metals Research Department
10 West 35th Street
Chicago, IL 60616
ATTN: Dr. N. Parikh

Kaiser Aluminum & Chemical Corp.
Aluminum Division Research Center
for Technology
P.O. Box 870
ATTN: T. R. Pritchett
Pleasanton, CA 94566

Kaman Aerospace Corporation
Old Windsor Road
Bloomfield, CT 06001
ATTN: Mr. M. L. White

Kawecki Berylco Industries
P.O. Box 1462
Reading, PA 19603

Linde Company
Division of Union Carbide
P.O. Box 44
Tonawanda, NY 14152

Lockheed Missile & Space Corp.
Box 504
Sunnyvale, CA 94088
ATTN: Mr. G. P. Pinkerton
Bldg. 154, Dept. 8122

Lockheed-Georgia Company
Marietta, GA 30061
ATTN: E. Bateh

Lockheed-California Company
P. O. Box 551
Burbank, CA 91503
ATTN: Mr. J. M. VanOrden
Dept. 74-71, Bldg. 221, Plt. 2

Lockheed Palo Alto Research Lab.
Materials Science Laboratory
3251 Hanover Street
Palo Alto, CA 94303
ATTN: Dr. Frank A. Crossley
52-31/204

R. E. Lewis
Lockheed Palo Alto Research Laboratory
Dept. 52-31
Bldg. 204
3251 Hanover Street
Palo Alto, CA 94304

P. R. Mallory & Co., Inc.
3029 East Washington Street
Indianapolis, IN 46206
ATTN: Technical Librarian

Martin Marietta Corporation
P. O. Box 5837
Orlando, FL 32805
ATTN: Dr. Richard C. Hall
Mail Point 275

Martin Marietta Corporation
1450 South Rolling Road
Baltimore, MD 21227
ATTN: Dr. Joseph R. Pickens

Martin Marietta Aluminum
ATTN: Mr. Paul E. Anderson
(M/C 5401)
19200 South Western Avenue
Torrance, CA 90509

McDonnell Aircraft Company
St. Louis, MO 63166
ATTN: Mr. H. J. Siegel
Materials & Processes Dev.
General Engineering Division

Midwest Research Institute
425 Volker Boulevard
Kansas City, MO 64110

Northrop Corporation
Aircraft Division
Dept. 3771-62
3901 West Broadway
Hawthorne, CA 90250
ATTN: Mr. Allen Freedman

Pratt & Whitney Aircraft
Division of United Technologies
Florida Research and Development Center
P.O. Box 2691
West Palm Beach, FL 33402

Dr. Howard Bomberger
Reactive Metals, Inc.
Niles, OH 44446

Reynolds Metals Company
Metallurgical Research Division
4th and Canal Streets
Richmond, VA 23219
ATTN: Dr. J. H. Dedrick

Reynolds Metals Company
Metallurgical Research Division
4th and Canal Streets
Richmond, VA 23219
ATTN: Mr. G. Spangler

Reynolds Metals Company
Metallurgical Research Division
4th and Canal Streets
Richmond, VA 23219
ATTN: Dr. D. Thompson

Rockwell International
P.O. Box 1082
1027 Camino Dos Rios
Thousand Oaks, CA 91320
ATTN: Dr. J. Wert

Rockwell International
Los Angeles Division
International Airport
Los Angeles, CA 90009
ATTN: Gary Keller
Materials Applications

Autonetics Division of
Rockwell International
P.O. Box 4173
Anaheim, CA 92803
ATTN: Mr. A. G. Gross, Jr.
Dept. 522-92

Rockwell International
Columbus Division
Columbus, OH 43216
ATTN: Mr. P. Maynard,
Dept. 75, Group 521

Solar
2200 Pacific Highway
San Diego, CA 92112
ATTN: Dr. A. Metcalfe

Southwest Research Institute
8500 Culebra Road
P. O. Box 28510
San Antonio, TX 78284

Teledyne CAE
1330 Laskey Road
Toledo, OH 43601

Vought Corp.
P. O. Box 5907
Dallas, TX 75222
ATTN: Mr. A. Hohman

Westinghouse Electric Company
Materials & Processing Laboratories
Beulah Road
Pittsburgh, PA 15235
ATTN: Don E. Harrison

Dr. D. J. Duquette
Materials Engineering Dept.
RPI
Troy, NY 12181

Dr. Charles Gilmore
Tompkins Hall
George Washington University
Washington, DC 20006

Dr. E. A. Starke, Jr.
Dept. of Materials Science
University of Virginia
Charlottesville, VA 22901

Dr. John D. Wood
Associate Professor
Lehigh University
Bethlehem, PA 18015